

NACA TN 4125 09701

TECH LIBRARY KAFB, NM
0066877

NATIONAL ADVISORY COMMITTEE FOR AERONAUTICS

TECHNICAL NOTE 4125

HEAT TRANSFER AND RECOVERY TEMPERATURES ON A SPHERE WITH
LAMINAR, TRANSITIONAL, AND TURBULENT BOUNDARY LAYERS

AT MACH NUMBERS OF 2.00 AND 4.15

By Ivan E. Beckwith and James J. Gallagher

Langley Aeronautical Laboratory
Langley Field, Va.



Washington
December 1957

AEM2C

TECHNICAL LIBRARY



TECHNICAL NOTE 4125

HEAT TRANSFER AND RECOVERY TEMPERATURES ON A SPHERE WITH

LAMINAR, TRANSITIONAL, AND TURBULENT BOUNDARY LAYERS

AT MACH NUMBERS OF 2.00 AND 4.15

By Ivan E. Beckwith and James J. Gallagher

SUMMARY

An investigation was made of the pressure and equilibrium-temperature distributions on a sphere at Mach numbers of 2.00 and 4.15. The local aerodynamic heat transfer was also measured on a sphere at a Mach number of 2.00 and on a hemisphere-cylinder at a Mach number of 4.15. The Reynolds number range for these tests was from 1.5×10^6 to 8.1×10^6 , based on free-stream conditions and the diameter of the spheres.

Measured equilibrium-temperature distributions over the forward part of the sphere agreed with a laminar theory at the lower Reynolds numbers and with a turbulent theory at the higher Reynolds numbers for both Mach numbers. At a Mach number of 2.00 the recovery temperatures in the separated-flow region decreased slightly with increasing Reynolds number.

Heat-transfer measurements at the stagnation point made at both Mach numbers agreed with laminar theory. At a Mach number of 2.00 transition to turbulent flow occurred at about 20° from the stagnation point. The heat-transfer coefficients in the turbulent boundary layer were in reasonably good agreement with a simple theory for this case. Similar results were obtained at a Mach number of 4.15 except that transition occurred farther back on the nose and, at the lower Reynolds numbers, the flow was laminar over the entire hemisphere. At Mach number 2.00 the heat-transfer coefficients in the separated-flow region were about 12 percent of the peak values on the front part of the sphere.

INTRODUCTION

The aerodynamic characteristics of blunt bodies at supersonic speeds have received considerable study in recent years. One of the principal reasons for this increased interest is the large reduction in local temperature that may be obtained by blunting the nose of a body. The

temperatures on the surface of a blunt nose are generally less than those on a sharp nose at given stream conditions because of the smaller aerodynamic heat-transfer rates, the increased heat-storage capacity, and the increased rate of heat removal by conduction in the blunt nose.

Several experimental and theoretical investigations of the aerodynamic heat-transfer characteristics of hemispherical noses or blunt bodies at supersonic speeds are reported in references 1 to 9. Most of the experimental data of these investigations were obtained at relatively small Reynolds numbers, and these data are generally found to be in reasonable agreement with theoretical predictions for a laminar boundary layer. Some measurements of the heat transfer in a turbulent boundary layer are reported in reference 2; however, more data are required before general correlations or comparisons with theoretical calculations for turbulent heat transfer are possible.

The purpose of this report is to present additional experimental data on recovery temperatures and aerodynamic heat transfer on spherical noses with laminar, transitional, and turbulent boundary layers. The tests were made at stream Mach numbers of 2.00 and 4.15 over a Reynolds number range from 1.5×10^6 to 8.1×10^6 , based on free-stream conditions and the diameter of the spheres. The laminar and turbulent data are compared with appropriate theories. Heat transfer and recovery temperatures measured on the back of spheres in the separated-flow region are also presented.

SYMBOLS

C_p	pressure coefficient
c_m	specific heat of model material
c_p	specific heat of air at constant pressure
D	diameter of model
e	emissivity
F	function of wall thickness and temperature distribution (eq. (5))
H	heat-transfer parameter, $\frac{q_w D}{k_{\infty} T_o \sqrt{\frac{\rho_{\infty} U_{\infty} D}{\mu_{\infty}}}}$

h	heat-transfer coefficient, $\frac{q_w}{T_r - T_w}$
k	thermal conductivity
l	radius of heat-meter flange
$l_h = l_p$	Width of air gap around plug
l_p	radius of heat-meter plug
M	Mach number
N_{Nu}	Nusselt number, $\frac{hx}{k_w}$
N_{Pr}	Prandtl number, $\frac{c_p \mu}{k}$
p	pressure
Q	total heat flow rate
q	heat flow rate per unit area
R_D	wall Reynolds number, $\frac{\rho_w U_\infty D}{\mu_w}$
R_x	local wall Reynolds number, $\frac{\rho_w u_{1x}}{\mu_w}$
R_∞	stream Reynolds number, $\frac{\rho_\infty U_\infty D}{\mu_\infty}$
r	radius of model
r_{av}	average radius of model wall, $\frac{r_w + r_1}{2}$
T	temperature
T_e	equilibrium temperature $\left(\frac{\partial T}{\partial t} = 0\right)$
T_r	recovery temperature $(q_w = 0)$
T_{ref}	reference temperature for radiation, taken as temperature of tunnel walls
t	time

U_{∞}	velocity ahead of bow shock
u	local velocity
u_1^*	dimensionless velocity gradient at stagnation point, $\left(\frac{du_1}{dx} \frac{D}{U_{\infty}} \right)_{x=0}$
W	specific weight of model material
x	longitudinal distance around models from stagnation point
y	normal distance from surface
δ	boundary-layer thickness
δ^*	displacement thickness of boundary layer, $\int_0^{\delta} \left(1 - \frac{\rho u}{\rho_1 u_1} \right) dy$
ϵ	flange thickness (see appendix)
η	recovery factor, defined by equation (10)
θ	angular distance around models measured from stagnation point in spherical polar coordinate system
θ^*	momentum thickness of boundary layer, $\int_0^{\delta} \frac{\rho u}{\rho_1 u_1} \left(1 - \frac{u}{u_1} \right) dy$
μ	dynamic viscosity
ρ	mass density
σ	Stefan-Boltzmann constant, 0.173×10^{-8} Btu/(hr) (ft ²) (°R ⁴)
τ	shear stress
ϕ	axisymmetric coordinate on models in spherical polar coordinate system
X	independent variable in heat-conduction equation for flange

Subscripts:

A,B two geometrically similar models

c	constantan
f	heat-meter flange
i	inside surface of model
m	material used in model
o	stagnation point
p	outside surface of heat-meter plug
s	separation point
st	stainless steel
T	location of transition
t	total
w	outside wall of model
∞	at infinity or ahead of bow shock
1	local value just outside boundary layer (unless otherwise noted)
2	reference point taken at $\theta = 90^\circ$ (unless otherwise noted)

A bar over a symbol indicates the ratio of any temperature to stagnation temperature.

A prime denotes values indicated by a heat meter.

APPARATUS

Description of Tunnels

This investigation of pressure distributions and heat-transfer characteristics on spheres was conducted in three of the blowdown jets in the Gas Dynamics Branch of the Langley Aeronautical Laboratory. These jets exhaust to atmospheric pressure and are supplied with air which is stored in a tank field at a maximum pressure of 5,000 pounds per square inch and a specific humidity of less than 1 part of water per million parts of air by weight. The air is reduced in pressure by automatic

regulators to the desired stagnation pressure, which can be held constant to within 1/2 percent. The stagnation temperature was also automatically regulated so that the maximum variation of this temperature with time was 1° F per minute. Pertinent information about the three blowdown jets used and the range of operating conditions available for the tests is given in the following table:

	M = 2 open jet	Variable Mach number closed jet	M = 4 jet
Stagnation pressure, lb/sq in. gage	90 to 140	30 to 140	220 to 500
Stagnation temperature, °F . . .	120 to 680	100 to 130	120 to 320
Test-section Mach number	2.00 ± 0.02	2.00 ± 0.03	4.15 ± 0.03
Reynolds number per foot	8.5×10^6 to 33.0×10^6	7.0×10^6 to 33.0×10^6	12.1×10^6 to 44.0×10^6
Test-section size, width by height, in.	9 by 9	9 by 9	12 by 13
Type of diffuser	None	Fixed	Fixed

Models and Instrumentation

Pressure-distribution model.- The model used to obtain the pressure distributions was a $3\frac{1}{2}$ -inch-diameter sphere supported by a $\frac{5}{8}$ -inch-diameter sting. A sketch of this model is not shown since the shape and size of the model and its sting support are the same as those of the copper heat-transfer model shown in figure 1(a). The pressure-distribution model was constructed of stainless steel and was provided with 35 pressure orifices installed along one longitudinal line at intervals of 5° from $\theta = -10^\circ$ to $\theta = 160^\circ$. The diameter of the orifices was 0.02 inch.

Mercury manometers were used for all pressures below 50 pounds per square inch gage, and Bourdon gages were used for pressures greater than this value.

Equilibrium-temperature models.- The models used to obtain the equilibrium temperatures were thin-shell spheres made of Inconel. Two

models of different wall thickness were used. One model was 3 inches in diameter with a wall thickness of $1/8$ inch and was used to obtain equilibrium-temperature data at Mach number 4.15 only. This same model was subsequently machined to a diameter of $2\frac{7}{8}$ inches, which resulted in a wall thickness of $1/16$ inch. This latter model was then used to obtain additional equilibrium-temperature data at Mach number 4.15 in order to investigate the effect of wall thickness on the measured equilibrium temperatures. The $2\frac{7}{8}$ -inch-diameter Inconel model was also used to measure equilibrium temperatures at Mach number 2.00. A sketch of the 3-inch-diameter model and its sting support is shown in figure 1(b) together with the location and method of installation of the 32 iron-constantan thermocouples in the sphere shell.

The temperatures were recorded on self-balancing potentiometers. A manual switching system was used so that all the model temperatures as well as the stagnation temperature of the air could be recorded on a single instrument. The accuracy of the potentiometers used was $1/4$ percent of full-scale deflection which was 200° F for the tests at Mach number 2 and 330° F for the tests at Mach number 4.

Isothermal heat-transfer model.- The isothermal heat-transfer model was a relatively thick-shell sphere made of electrolytic pure copper. The model was $3\frac{1}{2}$ inches in diameter and had a 0.3-inch-thick wall which remained essentially isothermal even for large heat-transfer rates because of the large thermal conductivity of copper. A sketch of the model, the sting support, and thermocouple installation is shown in figure 1(a). The thermocouples consisted of single constantan wires soldered at various locations on the model and a common heavy copper wire soldered at one point on the inside surface. As indicated in figure 1(a), 35 thermocouples were installed at 5° intervals along one longitudinal line with the copper-constantan junction located approximately 0.05 inch from the outside surface. Also, four thermocouples were attached to the inside surface at intervals of 45° . The model was chromium plated to reduce surface abrasion during the tests. The thickness of the chromium plating was approximately 0.0002 inch.

The temperature-time history of this model was obtained from a 36-channel recording oscillograph which has elements with a sensitivity of 12.8 microamperes per inch of deflection. Full-scale deflection was about $1\frac{1}{2}$ inches, which corresponded to a temperature change of 250° F. An accuracy in absolute temperature of 1° F was obtained by individually calibrating the galvanometer elements before each test. The relative temperatures from any one channel were accurate to within $\pm 1/4^{\circ}$ F. The

stagnation temperature was obtained from self-balancing recording potentiometers with an accuracy of $1/4$ percent of full-scale deflection. Two instruments were used with ranges of 0°F to 600°F and 0°F to $1,200^{\circ}\text{F}$ depending upon the range of the tests.

Hemisphere-cylinder heat-transfer model.- The hemisphere-cylinder model was 2 inches in diameter and had a wall thickness of 0.110 inch. The model was made of stainless steel and was instrumented with 7 plug-type heat meters and 10 copper-constantan thermocouples. The location of the thermocouples and heat meters and the construction of the heat meters are shown in figure 1(c). The meters were fabricated by first tinning the contact surfaces of the stainless steel and constantan with 0.0015 inch of silver solder and, then, heating the assembly under pressure to make the joints as thin as possible. The meters or plugs were then silver soldered into the model with a lower temperature solder and a final machining cut was made on the whole model. A flange that was 0.006 inch to 0.012 inch thick held the meters in place. The air space was sealed at the inside surface with insulating cement and the stainless-steel wires were spot welded to the meter and model.

The outside thermocouples were installed with the junction very near the surface. This installation was accomplished by first coating the bare thermocouple wires with a heat-resistant insulating paint. The individual wires were then inserted in separate holes drilled normal to the surface and spaced 0.1 inch apart, as indicated in figure 1(c). The ends of the wires were cut off flush with the outside surface and dressed down smooth. The thermoelectric circuit was then completed by a very thin film of silver solder applied over the outside surface area including the two holes.

Heat-transfer data were obtained on this model by cooling it with water at a constant flow rate and temperature until steady wall temperatures were indicated. The electromotive force across the constantan disk in the center of the heat meter is then proportional to the heat flow rate through the plug. Application of a correction factor to this heat flow rate gives the heat flow rate per unit area at the outside surface.

The output from the heat meters was amplified by a direct-current amplifier which has six different scales ranging from 50 microvolts to 2,000 microvolts full-scale deflection. The output from the amplifier was recorded on a self-balancing potentiometer. The overall accuracy of the amplifier and recorder is $1/2$ percent of full-scale deflection for a steady input.

TEST PROCEDURES AND DATA REDUCTION

Longitudinal heat conduction around the shells of the models and heat transfer due to radiation were included whenever necessary in the data reduction for the equilibrium-temperature models and the copper heat-transfer model. The relation used in data reduction is derived from the heat balance for an element of a spherical shell with small but finite wall thickness $\Delta r = r_w - r_i$ and volume $r_{av}^2 \sin \theta d\phi d\theta \Delta r$ where r_{av} is the average or mean radius of the shell. The aerodynamic heat-transfer rate for an axisymmetric temperature distribution and zero heat transfer at the inside surface is then:

$$q_w = Wc_m \Delta r \left(\frac{r_{av}}{r_w} \right)^2 \frac{\partial T}{\partial t} - \frac{k_m \Delta r}{r_w^2} \left(\frac{\partial^2 T}{\partial \theta^2} + \frac{1}{\tan \theta} \frac{\partial T}{\partial \theta} \right) + \sigma e (T_w^4 - T_{ref}^4) \quad (1)$$

where in this equation T should be considered as an average temperature across the thickness Δr at any station θ . A similar expression for the aerodynamic heat transfer to a spherical shell is given in reference 8 where no restriction is imposed on the shell thickness but the temperature derivatives with respect to time and θ are assumed independent of r . The temperature-time derivative term in the expression of reference 8 is, therefore, different from the corresponding term in equation (1). For the shell thickness and radius of the copper heat-transfer model this term in equation (1) is about 0.7 percent smaller than the exact value from reference 8.

A general procedure used in all the tests was to preheat the piping and tunnel system up to a temperature approximating the desired stagnation temperature. This procedure insured that for the equilibrium-temperature tests the heat-transfer rates due to radiation were small. The thermal properties of air were taken from reference 10.

Equilibrium and Recovery Temperatures

Thin-shell models.— The term "equilibrium temperature" is used to denote the local measured temperature when $\frac{\partial T}{\partial t} = 0$, and the term "recovery temperature" is used for the local temperature that would be obtained when the local value of $q_w = 0$. Before any equilibrium-temperature data were obtained, the tunnel was run at steady stagnation conditions for at least 5 minutes, and, as a result, the storage term of equation (1) was negligible. In general, when $\frac{\partial T}{\partial t} = 0$, $q \neq 0$ but has some small finite value

which is difficult to calculate accurately because the temperature derivatives in equation (1) are difficult to evaluate accurately from experimental data. The recovery temperatures may be obtained from the measured equilibrium temperatures on two thin-shell models of different wall thicknesses (without computing q_w from eq. (1)) by plotting the equilibrium temperature against wall thickness and extrapolating to zero thickness. In general, the correct functional form of the variation of equilibrium temperature with wall thickness is unknown; however, a simple linear extrapolation to zero thickness gives the recovery temperature with good accuracy as is shown by the following considerations.

If two thin-shell models, A and B, the same in every respect except for wall thickness and diameter, are tested in an airstream at the same Mach number M_∞ and Reynolds number $\frac{\rho_\infty U_\infty D}{\mu_\infty}$ and at nearly the same temperature, then dimensional considerations require that at corresponding points on the two models

$$\left(\frac{hD}{k_\infty}\right)_A = \left(\frac{hD}{k_\infty}\right)_B \quad (2)$$

The ratio of the local heat-transfer rates would then be

$$\frac{q_{w,A}}{q_{w,B}} = \frac{D_B}{D_A} \frac{k_{\infty,A}}{k_{\infty,B}} \frac{T_{w,A} - T_r}{T_{w,B} - T_r} \quad (3)$$

Solving this equation for T_r and substituting from equation (1) for the heat-transfer rates results in

$$\bar{T}_r = \frac{\bar{T}_{w,B} \frac{F_A}{F_B} - \bar{T}_{w,A}}{\frac{F_A}{F_B} - 1} \quad (4)$$

where all temperatures are made dimensionless by dividing by the test stagnation temperature. The ratio $\frac{F_A}{F_B}$ is given by the equation

$$\frac{F_A}{F_B} = \frac{\left(\frac{\Delta r}{Dk_\infty}\right)_A \left(\frac{\partial^2 \bar{T}}{\partial \theta^2} + \frac{1}{\tan \theta} \frac{\partial \bar{T}}{\partial \theta}\right)_A}{\left(\frac{\Delta r}{Dk_\infty}\right)_B \left(\frac{\partial^2 \bar{T}}{\partial \theta^2} + \frac{1}{\tan \theta} \frac{\partial \bar{T}}{\partial \theta}\right)_B} \quad (5)$$

for the conditions of $\frac{\partial \bar{T}}{\partial t} = 0$ and negligible radiation.

The percent error in recovery temperature due to an error in the ratio $\frac{F_A}{F_B}$ is

$$\frac{d\bar{T}_r}{\bar{T}_r} = \frac{\frac{\bar{T}_{w,A}}{\bar{T}_{w,B}} - 1}{\frac{F_A}{F_B} - \frac{\bar{T}_{w,A}}{\bar{T}_{w,B}}} \frac{1}{\frac{F_A}{F_B} - 1} d\left(\frac{F_A}{F_B}\right) \quad (6)$$

from equation (4) for given values of $\bar{T}_{w,A}$ and $\bar{T}_{w,B}$. Equation (6) then indicates that, for the conditions of $\bar{T}_{w,A} \approx \bar{T}_{w,B}$ and $F_A \neq F_B$, a rather large error in the ratio $\frac{F_A}{F_B}$ can be tolerated without causing a correspondingly large error in recovery temperatures. Consequently, when $D_A \approx D_B$ and $k_{\infty,A} \approx k_{\infty,B}$, equation (5) may be replaced by the approximate expression

$$\frac{F_A}{F_B} \approx \frac{\Delta r_A}{\Delta r_B} \quad (7)$$

since it follows from the conditions of $\bar{T}_{w,A} \approx \bar{T}_{w,B}$ and the physical similarity of the models that the temperature derivatives are also approximately equal. Substituting equation (7) into equation (4) results in the approximate expression for the recovery temperature ratio

$$\bar{T}_r \approx \frac{\bar{T}_{w,B} \frac{\Delta r_A}{\Delta r_B} - \bar{T}_{w,A}}{\frac{\Delta r_A}{\Delta r_B} - 1}$$

This expression shows that for thin-wall models the recovery temperature is given by a linear extrapolation to zero thickness of the variation in equilibrium temperature with wall thickness.

The radiation term was computed for some typical tests and was found to be less than 4 percent of the conduction term and, hence, was generally neglected. The small value of the radiation term is due to the relatively small values of T_w and T_{ref} and, also, to the fact that these temperatures were about the same because of the preheating before each test.

The physical constants for the Inconel used in the data reduction were $k_m = 8.5 \text{ Btu}/(\text{hr})(\text{ft})(^\circ\text{F})$ and $e = 0.2$. The models were polished between all tests.

Heat-meter model.— The aerodynamic heat-transfer rates were measured directly on this model so that the recovery temperatures were obtained by plotting H (proportional to q_w) against $\frac{T_o - T_w}{T_o}$ and extrapolating to $H = 0$; that is, for $H = 0$, $q_w = 0$ and $\frac{T_o - T_w}{T_o} = \frac{T_o - T_r}{T_o}$.

Transient Heat-Transfer Measurements

The aerodynamic heat transfer at Mach number 2.00 was obtained on the thick-wall copper sphere by a transient method. In this method the heat-storage or time-dependent term of equation (1) is usually the predominant factor in calculating the aerodynamic heat transfer. The model was protected from the unsteady starting conditions in the jet by disposable water-cooled covers. The covers consisted of double-walled hemispherical shells which were fitted together with a leak-proof seal. After attaining the desired steady conditions in the jet, a quick-release mechanism was actuated and the covers were blown off the model by the airstream. In this way the model was maintained at a uniform temperature until the covers were released. The data indicated that this initial temperature distribution was uniform to within 2°F over the entire region where temperatures were measured.

The temperature variation with time at two points on the copper sphere during a typical test is shown in figure 2(a). The complete temperature-time history up to 1 second from time zero for the same test is shown in figure 2(b). The initial temperature of the model for this test was 85°F as indicated in the figures. The outside temperatures were measured approximately 0.05 inch from the outside surface (fig. 1(a)) and the inside temperatures, denoted by the flagged symbols in figure 2(b), were measured at the inside surface.

Figure 2(a) shows that the temperature derivatives with respect to time at small values of t depend on the radial location. However, in the derivation of equation (1), it is assumed implicitly that the temperature derivatives are independent of the radial location. Consequently, any temperature data for $0 < t < 0.3$ were not used.

Figures 2(a) and 2(b) show that the temperature also varies considerably with radial location. This variation indicates that small errors in the depthwise location of the outside thermocouples would cause errors in the derivatives of T with respect to θ required in equation (1). These

errors were minimized by adjusting the time zero for each thermocouple record according to the radial location of the thermocouple. This adjustment was obtained by disregarding the early part of the records (generally, $t < 0.3$ second) and extending the temperature-time curves backwards to the initial temperature by using the same slope and curvature that was found at the larger times (generally, $t > 0.3$ second). This procedure is illustrated in figure 2(a) where the extended portions of the curves are shown as dashed lines. The intersection of each extended curve with the line for the initial temperature of the model was then taken as the adjusted "time zero" for that particular thermocouple location (this adjusted time zero in fig. 2(a) is at -0.12 second for the outside thermocouple and 0.16 second for the inside thermocouple), and the temperatures were then read again at the adjusted times. The result of using this procedure on the typical test of figures 2(a) and 2(b) is shown in figure 2(c). The adjusted temperatures derived from the inside thermocouples are now about the same as the adjusted outside temperatures and some of the apparent irregularities in the temperature distributions of figure 2(b) have been removed. This agreement indicates that the general procedure just described is valid, and plots of the type of figure 2(c) were then used to evaluate the derivatives of T with respect to θ required in equation (1). No data at $t > 0.6$ second were used from this model because of the increasing ratio of the conduction to storage terms at the larger times. This limitation minimized the errors involved in evaluating the conduction since the ratio of the conduction to storage terms was always less than about 0.3 for $t < 0.6$ second. The heat transfer due to radiation was found to be negligible as compared with the storage and conduction terms.

The physical constants for copper used in the data reduction were $W = 559$ lb/cu ft, $c_m = 0.0915$ Btu/(lb)(°F), $k_m = 220$ Btu/(hr)(ft)(°F), and $e = 0.5$. The model was polished before each test.

Direct Measurement of Heat Transfer

A plug-type heat meter was used for the direct measurement of aerodynamic heat-transfer rates on the hemisphere-cylinder model which was tested at Mach number 4.15. A general objection to the plug-type heat meter has been that the plug may cause large perturbations in the local wall temperatures of the model. These temperature perturbations in turn cause disturbances in the local boundary-layer characteristics and, also, may introduce extraneous heat-conduction effects in the plug itself. The heat meter and test procedure used in this investigation were designed to minimize these effects. The model was cooled with large amounts of water (about 100 pounds per minute) in the manner indicated in figure 1(c) and, thereby, a nearly uniform temperature was maintained at the inside surface of the plugs and surrounding model wall. The outside temperatures of the plug and surrounding model were also about the same because of the

relatively thin wall and because the materials used in the plug (constantan and stainless steel) were chosen so that the net thermal conductivity through the plug and model wall was nearly the same. The overall effect of the thin wall and large cooling rates was to cause most of the heat flow to take place in a direction normal to the wall in the model as well as the plug. The air space around the plug (see fig. 1(c)) forces a one-dimensional heat flow through the constantan disk. After steady temperatures have been attained, the total heat flow rate per unit area through the plug is then

$$q_t = k_c \frac{\Delta T_c}{\Delta r_c} \quad (8)$$

where ΔT_c is the temperature difference across the constantan disk and Δr_c is the thickness of the constantan disk. This temperature difference is obtained from the electromotive force appearing across the stainless-steel wires to the heat meter. (See fig. 1(c).) The thermoelectric output of the stainless steel and constantan junctions is known as a function of temperature from a previous calibration of the same materials.

The aerodynamic heat-transfer coefficient is given by the equation

$$h = \frac{q_t}{T_r - T_p'} \left(\frac{h}{h'} \right) \quad (9)$$

where $\frac{h}{h'}$ is a factor that corrects for the amount of heat transferred between the surface of the flange and the airstream and, also, for the amount of heat conducted into the flange from the model. Heat transfer due to radiation is not included in equation (9) since it was negligible in comparison with the aerodynamic heat transfer. The surface temperature of the plug T_p' is computed by assuming one-dimensional heat flow through the plug and by using the temperature measured at the inside surface. The temperature distribution along the surface of the flange determines the correction factor $\frac{h}{h'}$ and depends on the heat-transfer coefficient and the dimensions and thermal conductivity of the flange as well as the surface temperatures of the plug and model. The temperature distribution on the flange may be calculated from a differential equation which is derived in the appendix.

The data presented in this report have not been corrected for the flange effect because of possible experimental errors in the measured

temperatures T_w and T_p ; however, typical values of the correction factor and the effect of various parameters on the factor are given in the appendix.

Values of T_p , T_w , and T_i are shown for a typical test in figure 2(d). The temperatures T_w and T_i are measured on the outside and inside surfaces of the model at the locations indicated in figure 1(c). Possible errors in these measured temperatures and the derivation of equation (9) are also given in the appendix.

The physical constants for the constantan and stainless steel used for this model were $k_c = 12.8 \text{ Btu}/(\text{hr})(\text{ft})(^\circ\text{F})$ and $k_{st} = 9.3 \text{ Btu}/(\text{hr})(\text{ft})(^\circ\text{F})$, respectively. The stainless steel was type 303, that is, about 18 percent chromium and 9 percent nickel. The thermoelectric output of the particular stainless-steel-constantan combination used in this model is given in the following table:

Average temperature of junctions, $^\circ\text{F}$	Microvolts per $^\circ\text{F}$
60	27.5
80	25.4
100	24.2
120	23.4
140	23.1

This model was polished before most of the tests; however, several tests were made without polishing in order to observe the effect on the heat transfer of the natural-surface abrasion caused by foreign material in the airstream.

RESULTS AND DISCUSSION

Pressure Distributions

The variation of pressure coefficient C_p with θ at $M = 2.00$ for various stream Reynolds numbers is shown in figure 3. Over the front part of the sphere the pressure does not vary appreciably with Reynolds number and up to about $\theta = 60^\circ$ is closely approximated by the Newtonian distribution

$$C_p = C_{p,0} \cos^2 \theta$$

where $C_{p,0}$ was calculated from the average Mach number of the jet and the normal shock relations. On the back of the sphere within the separated-flow region the Reynolds number has a large effect on the pressure and also on the separation point.

A comparison of the separation point obtained from schlieren photographs of the recovery-temperature model with the separation point indicated by the pressure data of figure 3 is shown in figure 4. In general, the flow separates somewhat farther forward on the recovery-temperature model, as shown by the schlieren data, than on the pressure-distribution model. The different location of the separation points on the two models is probably caused by the different sting diameters or some other change in the flow associated with the particular jets used for the tests. The recovery-temperature model has a ratio of sting diameter to model diameter of 0.24 as compared with a ratio of 0.18 for the pressure-distribution model. (See figs. 1(b) and 1(a).) The schlieren photographs were taken of the recovery-temperature model in the variable Mach number closed jet and the pressure data were obtained in the $M = 2$ open jet with the nose of the model 7/8 inch inside the end of the jet. Sample schlieren photographs at three Reynolds numbers are shown as figure 5 to illustrate the rearward movement of the separation point with increasing Reynolds number. The location of separation was assumed to be at the point of intersection of the forward oblique shock with the surface of the sphere.

The pressure distributions obtained on the sphere at $M_\infty = 4.15$ and at $R_\infty = 6.7 \times 10^6$ and 9.1×10^6 are shown in figure 6. The pressure over the forward part of the model is in good agreement with that calculated by the Newtonian expression almost all the way to the separation point. This small change in Reynolds number had little effect on the separation pressure or location.

Equilibrium and Recovery Temperatures

$M_\infty = 4.15$. - The thin-wall Inconel model was tested first with a wall thickness of 1/8 inch at $M_\infty = 4.15$. After these tests were completed, the same model was machined to a wall thickness of 1/16 inch and more data were obtained. The results of both series of tests are presented in figure 7 where the ratios of the measured equilibrium temperatures to the stagnation temperatures T_e/T_0 are plotted against stream Reynolds number R_∞ for values of θ from -10° to 145° . On the front part of the sphere from the stagnation point to about $\theta = 35^\circ$, there is little dependence of T_e/T_0 on R_∞ (fig. 7(a)). From about $\theta = 35^\circ$ to $\theta = 115^\circ$ (figs. 7(b) to 7(d)), T_e/T_0 generally increases with Reynolds number R_∞ . For $\theta > 115^\circ$ (figs. 7(d) and 7(e)), T_e/T_0 is about constant when $R_\infty > 4.5 \times 10^6$. The values of T_e/T_0 are higher

on the thin-wall model than on the thick-wall model at all values of θ except in the range of θ from approximately 90° to 115° . This temperature reversal is caused by the increased heat conduction into this region on the thick-wall model since the minimum temperatures are found here.

Transition occurred at $R_\infty \approx 4.5 \times 10^6$ at all values of $\theta > 45^\circ$ as indicated by the abrupt increase in T_e/T_0 on the thin-wall model at this Reynolds number. For values of $\theta > 115^\circ$ and $R_\infty < 4.0 \times 10^6$, the measured temperatures on the thick-wall model may be about 1 percent too low because of insufficient testing time to allow for the extremely low heating rates in this region.

The data shown in figure 7 have been extrapolated linearly to zero wall thickness since, according to the discussion in the section entitled "Thin-shell models," this procedure is permissible if $\bar{T}_{w,A} \approx \bar{T}_{w,B}$ and $D_A \approx D_B$. The results of the extrapolation are shown in figure 8 where the ratio of the recovery temperature to the stagnation temperature T_r/T_0 is plotted against θ for three Reynolds numbers. The curves labeled "laminar theory" and "turbulent theory" were computed from the relation

$$\frac{T_r}{T_0} = \eta \left(1 - \frac{T_1}{T_0} \right) + \frac{T_1}{T_0} \quad (10)$$

where $\eta = \sqrt{N_{Pr}}$ for the laminar-flow theory, $\eta = \sqrt[3]{N_{Pr}}$ for the turbulent-flow theory, and the Prandtl number was assumed constant at $N_{Pr} = 0.7$. Just as is shown in figure 7, these data are almost independent of R_∞ for $\theta < 40^\circ$, and at $R_\infty = 3.0 \times 10^6$ the data are slightly below the laminar-theory curve. For $\theta > 40^\circ$, T_r/T_0 at the larger Reynolds numbers is higher than the laminar data and tends to follow the trend of the turbulent-theory curve. This behavior indicates that transition occurred at about $\theta = 40^\circ$ to 45° . Downstream of the separation point which was between $\theta = 90^\circ$ and 105° (in agreement with the pressure data of fig. (6)) T_r/T_0 is again independent of R_∞ and increases with increasing distance around the model. All the data up to $\theta = 90^\circ$ would be in better agreement with the theory if the laminar-theory and turbulent-theory curves were reduced about 1 percent in order to agree with the data at $\theta = 0^\circ$.

Some recovery-temperature data from the heat-meter model are also shown in figure 8. These data were obtained from figure 9 where the dimensionless heat-transfer parameter H is plotted against the temperature parameter $\frac{T_0 - T_w}{T_0}$. In accordance with a procedure given in the

section entitled "Heat-meter model," the recovery temperatures from this figure are computed from the intersection of the faired curves with the axis $H = 0$ so that the expression for T_r/T_o is

$$\frac{T_r}{T_o} = 1 - \left(\frac{T_o - T_w}{T_o} \right)_{H=0}$$

Note, however, that the surface temperature distribution on the heat-meter model is such that the condition $q_w = 0$ is generally found at only one point or area on the model during any one test. Thus, in figure 9 the points to the extreme left (smallest values of $\frac{T_o - T_w}{T_o}$) were all obtained in the same test, so that for this test $q_w \approx 0$ at $\theta = 75^\circ$ and 90° ; for $\theta < 75^\circ$ the wall temperatures were still considerably below recovery temperatures. According to a qualitative analysis of the effect of wall temperature distribution on the local recovery temperatures, the recovery temperatures from figure 9 should then be somewhat less than the values on the thin-wall spheres where for any one test $q_w \approx 0$ over the entire model. Comparison of the data in figure 8, however, shows good agreement between the two sets of data at comparable Reynolds numbers. Apparently, then, this effect is too small to be measured in the present tests.

$M_\infty = 2.00$.-- The ratio of the equilibrium temperature to the stagnation temperature T_e/T_o measured at a stream Mach number of 2.00 is presented in figure 10. These data were all obtained on the Inconel model with a wall thickness of 1/16 inch. On the front part of the sphere the results are similar to the recovery-temperature data at $M_\infty = 4.15$ (fig. 8) except that for the larger Reynolds numbers ($R_\infty \geq 6.45 \times 10^6$) transition apparently occurred somewhat farther forward at $\theta \approx 25^\circ$ to 30° . At the lower Reynolds numbers ($R_\infty \leq 3.49 \times 10^6$) transition apparently occurs ahead of $\theta = 90^\circ$ as indicated by the increasing values of T_e/T_o in the vicinity of $\theta = 70^\circ$ to 80° .

The theoretical curves were computed by use of equation (10) with the same values of η . The agreement between the data and the theory would be improved if the theoretical values were reduced by about 1/2 percent.

In the separated region (fig. 10), T_e/T_o was essentially constant with increasing distance around the model but decreased slightly with increasing Reynolds number. This decrease is probably caused by the same

flow mechanism which caused the corresponding decrease in the pressure in the separated region shown in figure 3.

Heat-Transfer Coefficients

Stagnation point.- All the heat-transfer data obtained at the stagnation point in this investigation are shown in figure 11 as a "wall" Nusselt number $\frac{hD}{k_w}$ plotted against a parameter which is the product of a "wall" Reynolds number $R_D = \frac{\rho_w U_\infty D}{\mu_w}$ and the dimensionless velocity gradient u_1^* evaluated at the stagnation point. The recovery temperatures used to compute h were taken from the data of figures 8 and 10. The heat-transfer data at $M_\infty = 2.0$ were obtained on the thick-wall copper sphere by the transient method, and the data at $M_\infty = 4.15$ were obtained on the hemisphere-cylinder model with the heat meters. The heat-meter data are shown uncorrected for any errors caused by the heat transferred to the flange. Some of the data at $M_\infty = 4.15$ were obtained with the hemisphere-cylinder model yawed 15° in order to provide a cross check of the heat-transfer coefficients obtained from the different meters. Comparison of these data shows that the heat meter located at $\theta = 15^\circ$ in the unyawed position and at $\theta = 0^\circ$ when the model was yawed (see fig. 1(c)) was indicating heat-transfer rates about 10 percent higher than the meter at $\theta = 0^\circ$ (model unyawed). This discrepancy is probably caused by constructional variations in the plugs since yawing the model should have no effect on the heat transfer on the hemispherical nose.

Lines shown in figure 11 labeled "laminar theory" are computed from the results of reference 9 where it is shown that in the vicinity of the stagnation point the local Nusselt number divided by the square root of the local Reynolds number or the quantity

$$\frac{h}{k_w \sqrt{\frac{\rho_w}{\mu_w} \frac{u_1}{x}}}$$

is a function only of the Prandtl number and the ratio of wall temperature to stagnation temperature. If the dimensionless velocity gradient at the stagnation point u_1^* is introduced into this quantity, then

$$\frac{hD}{k_w} = \left(\frac{N_{Nu}}{\sqrt{R_x}} \right) \left(\frac{\rho_w U_\infty D}{\mu_w} u_1^* \right)^{\frac{1}{2}} \quad (11)$$

The values used for $\frac{N_{Nu}}{\sqrt{R_x}}$ were 0.663 and 0.639, respectively, for $T_w/T_o = 1.0$ and 0.5 (ref. 9). The values used for u_1^* were 1.54 for $M_o = 2.00$ and 1.19 for $M_o = 4.15$, as obtained from the pressure-distribution data of figures 3 and 6.

The data at $M_o = 2.00$ are in good agreement with the theory but the data at $M_o = 4.15$ are about 12 percent higher than the theory. Application of a correction for flange effects would reduce these data at $M_o = 4.15$ by 15 to 25 percent; this reduction depends on the plug and wall temperatures and flange thickness, as discussed in the appendix. Apparently, then, the corrected data at $M_o = 4.15$ would be somewhat lower than the theory by an amount which is well within the uncertainties due to flange correction and constructional variations in the plugs. No effect of a variation in T_w/T_o as indicated by the theory could be detected in the data.

Variation of heat-transfer coefficients with θ at $M_o = 2.00$.

The heat-transfer coefficients on the copper sphere at $M_o = 2.00$ are presented in figure 12 as the ratio of the local heat-transfer coefficient to the value at the stagnation point. The local heat-transfer rates were calculated from the experimental temperature-time histories by using equation (1), and the recovery temperatures were obtained from the experimental data of figure 10.

The large increases in heat transfer occurring on the front part of the sphere and reaching a maximum at about $\theta = 40^\circ$ (fig. 12) are evidently caused by transition to turbulent flow, since the heat-transfer coefficients at the stagnation point are in agreement with laminar theory (fig. 11). Also, if the boundary layer were entirely laminar, the heat transfer would be expected to decrease with increasing θ as shown in previous investigations. (See, for example, refs. 4 and 8.)

The heat-transfer distribution for a laminar boundary layer, as shown in figure 12, was computed from the method of reference 11 by use of Mangler's transformation (ref. 12). Comparison of the theory with the experimental data shows reasonably good agreement from the stagnation point up to the region of $\theta = 10^\circ$ to 30° where large increases in h occurred. This value of θ is presumably the location for the beginning of transition and is subsequently referred to as θ_T .

The theoretical heat-transfer distribution in a turbulent boundary layer was computed by using a modification of Falkner's expression (ref. 13) for the skin friction on a flat plate given by the equation

$$\frac{\tau_w}{\rho_w u_1^2} = \frac{0.0131}{\left(\frac{\rho_w u_1 x}{\mu_w}\right)^{1/7}}$$

and Reynolds analogy in the form

$$\frac{h}{\rho_w u_1 c_p} = 1.2 \frac{\tau_w}{\rho_w u_1^2}$$

where the gas properties are evaluated at the local wall temperature and local pressure. (Skin-friction coefficients and Reynolds analogy from these formulas are compared with recent experimental data on flat plates at supersonic speeds in refs. 14 and 15.) The resulting expression for the heat-transfer coefficient is

$$h = 0.0157 \frac{\rho_w u_1 c_p}{\left(\frac{\rho_w u_1 x}{\mu_w}\right)^{1/7}} \quad (12)$$

Combining equation (12) with the expression for the laminar heat-transfer coefficient at the stagnation point obtained from equation (11) and assuming constant T_w gives the equation

$$\frac{h}{h_{\theta=0}} = \frac{0.0157 N_{Pr}}{\sqrt{u_1} \left(\frac{N_{Nu}}{\sqrt{R_x}}\right)_{x=0}} \frac{\left(\frac{p_1}{p_{1,0}} \frac{u_1}{U_\infty}\right)^{6/7}}{\left(\frac{x}{D}\right)^{1/7}} \frac{\left(\frac{\rho_w U_\infty D}{\mu_w}\right)^{5/14}}{x=0} \quad (13)$$

which was used to compute the long-short-dash curves in figure 12 labeled "local flat plate (turbulent theory)." The local values of pressure and velocity were obtained from the measured pressure distributions of figure 3 and x was measured from the stagnation point. The two curves shown were computed for $R_D = 11 \times 10^6$ and 19×10^6 which are the

approximate limits of this parameter for the tests. Comparison of the experimental data with the theory indicates that equation (13) predicts the correct variation of the heat transfer with θ from $\theta = 40^\circ$ to 90° . The predicted magnitude of the heat transfer on this portion of the model is generally conservative. The experimental values are as much as 20 percent below the computed values except for the test at $R_\infty = 2.74 \times 10^6$ where the data are as much as 40 percent below the theory. The agreement between the experimental data and the theory indicates that, within the experimental scatter of the present data, the simple flat-plate formulas given by equation (12) predict the turbulent heat transfer on spheres with reasonable accuracy. No consistent trend caused by changes in R_D or T_w/T_0 is evident in the data. The experimental scatter in the data is probably masking any such effects over the small range of Reynolds number and temperature available in these tests. The heat-transfer coefficients in the separated region on the back of the sphere are about 12 percent of the peak turbulent values.

Heat-transfer coefficients at $M_\infty = 4.15$.— The experimental heat-transfer coefficients on the hemisphere-cylinder model at $M_\infty = 4.15$ are presented in figure 13 in the form of the wall Nusselt number divided by the square root of the wall Reynolds number. This particular parameter was used here rather than $h/h_{\theta=0}$ in order to correlate the laminar heat-transfer data and, also, to facilitate comparison with other experimental and theoretical investigations, such as those of references 4 and 9. The heat-transfer rates were obtained directly from the heat-meter readings by means of equation (8) with no correction included for flange effects. (See the appendix for a discussion of these corrections.) The recovery temperatures were obtained from the data of figure 8 and the local flow quantities were computed from the pressure distributions of figure 6 and the measured wall temperatures. Each data point shown in figure 13 is the arithmetic average of the values obtained from the number of tests indicated in the key.

The curves shown in figure 13 for the heat transfer in a laminar boundary layer were obtained by computing the variation in heat transfer around the sphere by the method of reference 11 and applying a correction to these results in order to bring the stagnation-point value into agreement with the theory of reference 9. The local flow quantities needed in this calculation were computed from the experimental pressure-distribution data of figure 6.

The theoretical distribution of the laminar heat-transfer parameter $hx/k_w \sqrt{\rho_w u_1 x / \mu_w}$ in a turbulent boundary layer is obtained from equation (12) and is given by the relation

$$\frac{hx}{k_w \sqrt{\frac{\rho_w u_1 x}{\mu_w}}} = (0.0157) N_{Pr} \left[\frac{u_1 p_1 x}{(u_1 p_1 x)_2} \right]^{5/14} \left(\frac{\rho_w u_1 x}{\mu_w} \right)_2^{5/14}$$

for $T_w = T_{w,2}$. The subscript 2 denotes quantities evaluated at any convenient reference point which in this case is taken at $\theta = 90^\circ$.

The data of figure 13 have been divided into two sets according to the condition of the model surface during the tests. One set of data was obtained when the model was carefully polished before each test. These data are designated by the open symbols in figure 13 and are considered representative of a "smooth" surface. The other set of data, designated by the solid symbols, was obtained when no attempt was made to keep the model polished and are considered representative of a "rough" surface. This latter procedure resulted in a considerably rougher model surface than the former procedure because of the cumulative effect during the tests of the natural abrasion caused by foreign material in the airstream.

In figure 13 a comparison of the data for a smooth surface (model polished before each test) with the laminar theory indicates that, when $R_\infty \leq 3.3 \times 10^6$, the data are about 15 to 30 percent higher than the theory but tend to decrease with increasing θ by about the same amount as the theory. For $R_\infty = 4.9 \times 10^6$, however, the values of the heat-transfer parameter at $\theta = 45^\circ$, 60° , and 75° are from 50 to 200 percent greater than the laminar theory and tend to approach the level predicted by the turbulent theory. Apparently, transition from laminar to turbulent boundary layer occurred between $\theta = 30^\circ$ and 45° at the larger Reynolds number. Note that alternate meters are located on opposite sides of the model (fig. 1(c)) so that if turbulent flow existed on one side of the model only, then alternate meters would indicate higher heat transfer.

The data for the rough surface (model unpolished) are, in general, higher than the other data in figure 13 except at $\theta = 0^\circ$ and 15° . At $\theta = 30^\circ$, 45° , and 75° for the lowest Reynolds number, these data are about 15 percent higher than the corresponding data from the smooth surface. As the Reynolds number is increased, the heat transfer tends to get progressively larger for all values of $\theta \geq 30^\circ$ and approaches the levels predicted by the turbulent theory. The data at $\theta = 90^\circ$ are, in general, below the turbulent theory. This may be attributed to two factors.

One of the factors is that the meter at $\theta = 90^\circ$ is not exposed to erosion effects to the same extent as the other meters and, hence, the local surface would not be as rough. Also, the small measured values of the heat-transfer rates at $\theta = 90^\circ$, as shown for typical conditions in figure 9, result in larger errors in the heat-transfer coefficient at this location since the instrumentation errors, as discussed in the appendix, would have a larger effect.

Application of a flange correction (see the appendix) would reduce all these data by 15 to 25 percent. This correction would bring the smooth-surface data at the smaller Reynolds numbers into good agreement with the laminar theory. The higher values of the heat transfer on the rough surface would be within the upper and lower limits of the turbulent theory. Evidently all other values of the heat transfer are in the transitional range. If the larger experimental values are for a fully turbulent boundary layer, then the flat-plate formulas again predict conservative values of the heat transfer.

Typical values of heat-transfer rates obtained on the hemisphere-cylinder model at $R_\infty = 3.3 \times 10^6$ and $M_\infty = 4.15$ are shown in figure 9. In order to correlate the data for a laminar boundary layer, the dimensionless parameter H is plotted against the temperature parameter $\frac{T_o - T_w}{T_o}$. The slope of the faired lines would be the local stream Nusselt number divided by the square root of the stream Reynolds number, and the value of the temperature parameter when $q_w = 0$ would be $\frac{T_o - T_r}{T_o}$. The relative scatter at $\theta = 60^\circ$, 75° , and 90° is greater than at $\theta = 0^\circ$, 15° , 30° , and 45° . This is probably caused by the greater sensitivity of the flow to surface roughness at the rearward stations. The heat-transfer-coefficient data presented in figures 11 and 13 were not derived from plots of the type shown in figure 9 since a larger number of tests at a given Reynolds number is then required in order to evaluate the Nusselt number.

Effect of Roughness on Transition

The quantitative effect of roughness on transition cannot be determined from the present tests since no attempt was made to measure or control the actual roughness. Some qualitative information may be gained from the tests, however, by calculating displacement and momentum thicknesses for comparison with the possible roughness present. Also, momentum-thickness Reynolds numbers at transition may be useful for comparison with other data.

The displacement and momentum thicknesses of the laminar boundary layer on a sphere have been calculated by the method of reference 16 by use of the experimental pressure distributions of figures 3 and 6. The displacement thickness times the square root of the wall Reynolds number was found to be almost constant over the first 30° of the sphere; that is,

$$\frac{\delta^*}{D} \left(\sqrt{\frac{\rho_w U_\infty D}{\mu_w}} \right)_{x=0} \approx 0.5$$

for $\theta < 30^\circ$ and for the range of Mach numbers and wall temperatures of the present tests. For the maximum Reynolds number range and the diameters applying to the heat-transfer tests at Mach numbers 2.00 and 4.15, the minimum value of δ^* is about 0.0003 inch and the maximum value is about 0.0005 inch on both sets of tests. These small values indicate that very small roughness heights of the order of 0.0002 inch would reduce considerably the transition Reynolds numbers if correlations obtained at low speed (ref. 17) of the effect of roughness can be applied to the subsonic flow region on the sphere. Observations made of the abrasion damage to the surface of the various models indicated that, in spite of polishing before the tests, at least this amount of roughness was present after the tests. The relative damage to the models was, in general, the greatest on the copper model and the least on the Inconel recovery-temperature models.

The Reynolds numbers for transition based on the local momentum thickness θ^* and the local flow quantities at the edge of the boundary layer are plotted against angular distance around the model in figure 14 for all the data obtained in this investigation. The location of transition was arbitrarily taken as the point where the heat-transfer coefficient or recovery temperature first began to increase from the nominal laminar values. Figure 14 shows that most of the data from the heat-transfer models with the rough surface (model unpolished) at $M_\infty = 2.00$ and at $M_\infty = 4.15$ are lower than the rest of the data and correlate approximately on one line. For these particular tests, this line apparently represents a minimum critical Reynolds number below which the flow was laminar. The data above this line are, in general, from the polished-model data at $M_\infty = 4.15$ and from the data for the recovery-temperature models. The two points plotted at $\theta = 90^\circ$ are from the smooth-surface model for $R_{\theta^*} \leq 3.3 \times 10^6$ and are included to show that transition occurred downstream of $\theta = 90^\circ$ for these conditions. All the data indicate that $R_{\theta^*,T}$ tends to increase with increasing θ .

CONCLUDING REMARKS

An investigation was made of the pressure and equilibrium-temperature distributions on a sphere at Mach numbers of 2.00 and 4.15. The local aerodynamic heat transfer was also measured on a sphere at Mach number 2.00 and on a hemisphere-cylinder at Mach number 4.15. The maximum Reynolds number range for these tests was from 1.5×10^6 to 8.1×10^6 , based on free-stream conditions and the diameter of the sphere.

The pressure distributions on the front part of the sphere were independent of the Reynolds number and in good agreement with the theoretical Newtonian distributions at both Mach numbers. At the lower Mach number the location of separation and the pressures in the separated-flow region were affected by the Reynolds number.

The equilibrium temperatures on the front part of the sphere at both Mach numbers were about 1 percent lower than those predicted by a simple theory which assumes that the local recovery factor (defined in terms of the local static temperature) is the square root of the Prandtl number for laminar flow and the cube root of the Prandtl number for turbulent flow. The data at the lower Reynolds numbers agreed with the trend given by the theory for laminar flow. As the Reynolds number was increased, the temperatures tended to increase and agreed more closely with the theory for turbulent flow.

Downstream from the separation point the recovery temperatures for the tests at Mach number 4.15 increased with increasing distance around the sphere and were practically independent of Reynolds number. At Mach number 2.00 the equilibrium temperatures were more nearly constant in the separated-flow region and decreased slightly with increasing Reynolds number.

The heat-transfer coefficients at the stagnation point from the tests at both Mach numbers were in good agreement with the theory of Reshotko and Cohen (NACA Technical Note 3513). The velocity gradients used in the theory were evaluated from the experimental pressure data.

The local heat-transfer coefficients from the tests at Mach number 2.00 were in agreement with the theory for laminar flow in the region up to approximately 20° from the stagnation point. Large increases in heat-transfer coefficient caused by transition to turbulent flow occurred beyond this region with the maximum values observed at about 40° from the stagnation point. From this location back to the separation point the approximate level in the heat-transfer coefficient as well as the variation with distance was fairly well predicted by a simple theory based on

turbulent heat-transfer formulas for flat plates. The heat-transfer coefficients in the separated-flow region were about 12 percent of the peak turbulent values on the front part of the sphere.

The heat-transfer coefficients from the tests at Mach number 4.15 at the higher Reynolds numbers were generally similar to the results at Mach number 2.00, except that transition usually occurred farther back on the nose. The maximum values of the heat-transfer coefficient downstream of transition were again in reasonably good agreement with the simple turbulent-flow theory. For Reynolds numbers of about 3.0×10^6 or less, the data over the entire hemispherical nose were in agreement with the theory for laminar flow.

Langley Aeronautical Laboratory,
National Advisory Committee for Aeronautics,
Langley Field, Va., August 6, 1957.

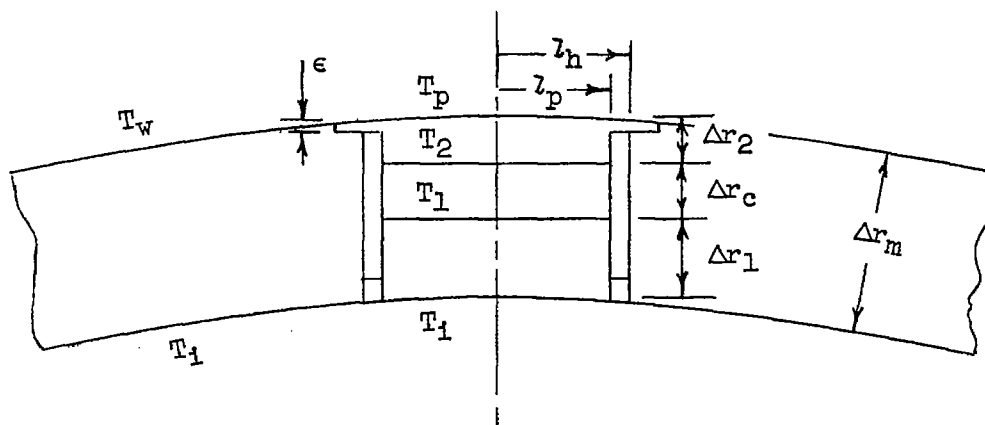
APPENDIX

HEAT-METER CORRECTIONS

The largest error in the heat-meter data is caused by heat conduction in the metal flange which bridges the gap between the plug and the model (fig. 1(c)). The external surface of this flange is exposed to approximately the same unit heat-transfer rates as the plug and model surface. The insulating properties of the air gap force this heat to flow into the plug or the surrounding model. The actual quantity of heat conducted into the plug from the flange depends on the temperature distribution in the flange and the temperatures of the plug and model. The indicated heat-transfer rate as obtained directly from the temperature drop across the constantan disk is then corrected by an amount which depends essentially on the difference in the actual surface area involved in the total heat flux through the plug and the projected area of the disk.

Ratio of Corrected to Indicated Heat-Transfer Coefficients

A section of a heat meter with symbolic notations is shown in sketch 1:



Sketch 1

The total heat Q_t flowing per unit time through the constantan disk of thickness Δr_c is the sum of Q_p into the surface area of the plug (the projected area of the constantan disk) and Q_f conducted in from the flange; that is,

$$Q_t = Q_p + Q_f \quad (A1)$$

where

$$\left. \begin{aligned} Q_t &= k_c \frac{\Delta T_c}{\Delta r_c} \pi l_p^2 \\ Q_p &= h(T_r - T_p) \pi l_p^2 \\ Q_f &= k_{st} \left(\frac{dT}{dl} \right)_{l=l_p} 2\pi l_p \epsilon \end{aligned} \right\} \quad (A2)$$

The temperature gradient $\frac{dT}{dl}$ is assumed constant across the flange thickness ϵ .

An "indicated" heat-transfer coefficient is defined as

$$h' = \frac{k_c \frac{\Delta T_c}{\Delta r_c}}{T_r - T_p'} \quad (A3)$$

where T_p' is the surface temperature of the plug, which is calculated by assuming one-dimensional heat flow through the entire plug. The ratio of the indicated heat-transfer coefficient to the true value is then obtained by combining equations (A1), (A2), and (A3). This ratio is

$$\frac{h'}{h} = \frac{T_r - T_p}{T_r - T_p'} \left[1 + \frac{2}{\chi_p^2} \frac{l_p}{1 - \frac{T_p}{T_r}} \frac{d}{dl} \left(\frac{T}{T_r} \right)_{l=l_p} \right] \quad (A4)$$

where

$$\chi_p = \sqrt{\frac{h}{k_{st}\epsilon}} l_p$$

From the notation shown in sketch 1 and the assumption of one-dimensional heat flow, the value of T_p' is given by the relation

$$T_p' = \left(1 + \frac{k_c}{k_{st}} \frac{\Delta r_1 + \Delta r_2}{\Delta r_c} \right) \Delta T_c + T_1 \quad (A5)$$

where $\Delta T_c = T_2 - T_1$. A more accurate value of T_p may be computed from equation (A4) by assuming that

$$h \equiv \frac{Q_p}{(T_r - T_p)\pi l_p^2} \approx \frac{k_{st}(T_p - T_2)}{\Delta r_2(T_r - T_p)} \quad (A6)$$

and by substituting equation (A3) for h' . The result is

$$T_p = T_2 + \frac{k_c}{k_{st}} \frac{\Delta r_2}{\Delta r_c} \Delta T_c \frac{1}{\lambda} \quad (A7)$$

where

$$\lambda = 1 + \frac{2}{\chi_p^2} \frac{l_p}{1 - \frac{T_p}{T_r}} \frac{d}{dl} \left(\frac{T}{T_p} \right)_{l=l_p} \quad (A8)$$

and from sketch 1

$$T_2 = \left(1 + \frac{k_c}{k_{st}} \frac{\Delta r_1}{\Delta r_c} \right) \Delta T_c + T_1 \quad (A9)$$

Subtracting equation (A7) from equation (A5) and using equation (A9) then gives

$$T_p' - T_p = \Delta T_c \frac{k_c}{k_{st}} \frac{\Delta r_2}{\Delta r_c} \left(1 - \frac{1}{\lambda} \right) \quad (A10)$$

Adding $(T_r - T_p')$ to both sides of equation (A10) and using equation (A3) for ΔT_c results in the expression

$$\frac{T_r - T_p}{T_r - T_p'} = 1 + \frac{\Delta r_2}{k_{st}} \left(1 - \frac{1}{\lambda} \right) h' \quad (A11)$$

The correction factor $\frac{h'}{h}$ is calculated from equations (A4) and (A11) for known values of h' and λ . An iterative procedure is necessary since λ is a function of h and $\frac{T_p}{T_r}$.

Temperature Distribution on the Flange

The temperature gradient $\frac{dT}{dz}$ at the inside edge of the flange depends on the quantity of heat transferred to the flange from the air-stream and the surrounding model as well as the thermal conductivity of the flange and its dimensions. These effects may be approximately accounted for by writing the heat balance for an element of the flange of width dz and assuming a constant temperature across the thickness ϵ of the flange. The heat-transfer coefficient h and the recovery temperature T_r are assumed constant throughout. The resulting differential equation is

$$\frac{d^2}{dz^2}(T_r - T) + \frac{1}{z} \frac{d}{dz}(T_r - T) - \frac{h}{k_{st}\epsilon}(T_r - T) = 0 \quad (A12)$$

with the boundary conditions of

$$\left. \begin{aligned} z &= z_p & T &= T_p \\ z &= z_h & T &= T_w \end{aligned} \right\} \quad (A13)$$

Introducing the independent variable

$$\chi = \sqrt{\frac{h}{k_{st}\epsilon}} z$$

into equation (A12) results in

$$\frac{d^2}{d\chi^2}(T_r - T) + \frac{1}{\chi} \frac{d}{d\chi}(T_r - T) - (T_r - T) = 0 \quad (A14)$$

which has the general solution

$$\frac{T}{T_r} = 1 - C_1 I_0(x) - C_2 K_0(x) \quad (A15)$$

where I_0 and K_0 are modified Bessel functions of the first and second kind of order zero and C_1 and C_2 are arbitrary constants chosen to satisfy the boundary conditions (eqs. (A13)). Note that these boundary conditions imply a discontinuity in temperature gradient at the edges of the flange since $\frac{dT}{dz} = 0$ for $l_p > l > l_h$ and no boundary conditions for the values of $\frac{dT}{dz}$ on the flange are imposed. It is believed, therefore, that the results obtained by using the boundary conditions (eqs. (A13)) are conservative since the physical requirement of a continuous temperature gradient would tend to reduce the temperature gradient at the inside edge of the flange and, thereby, to decrease the quantity of heat conducted into the plug from the flange.

The temperature gradient as obtained from equation (A15) is

$$\frac{d}{dz} \left(\frac{T}{T_r} \right)_{z=l_p} = \frac{x_p}{l_p} \left[-C_1 I_1(x_p) + C_2 K_1(x_p) \right] \quad (A16)$$

where I_1 and K_1 are modified Bessel functions of the first and second kind of order one. The quantity λ then becomes

$$\lambda = 1 + \frac{2}{x_p \left(1 - \frac{T_p}{T_r} \right)} \left[-C_1 I_1(x_p) + C_2 K_1(x_p) \right] \quad (A17)$$

The reciprocal of λ is plotted against $\frac{T_w - T_p}{T_r - T_p}$ in figure 15 for typical values of x_p .

Values of h' , $x_p' = \sqrt{\frac{h'}{k_{st}\epsilon}} l_p$, and $\frac{T_w - T_p'}{T_r - T_p'}$ from the test shown in figure 2(d) are given in the following table:

①	②	③	④	⑤	⑥	⑦	⑧	⑨	
θ , deg	ϵ , in.	$\frac{h',Btu}{(\text{sec})(\text{ft}^2)(^\circ\text{F})}$	x_p'	$\frac{T_w - T_p'}{T_r - T_p'}$	$\frac{1}{\lambda}$ (Fig. 15 and col. ④)	$\frac{T_r - T_p}{T_r - T_p'}$ (Eq. (A11))	$\frac{h}{h'}$ (Eq. (A18))	$\frac{T_w' - T_p'}{T_r - T_p'}$	$\frac{h}{h'}$
15	0.006	0.0543	1.068	0.034	0.63	1.018	0.619	0.018	0.71
15	.003	.0543	1.510	.034	.73	1.013	.720	.018	.78
45	.006	.0375	.887	.024	.63	1.012	.623	.013	.71
75	.006	.0144	.549	.015	.53	1.006	.527	.004	.74

The corresponding values of λ (obtained from fig. 15 and column ④), $\frac{T_r - T_p}{T_r - T_p'}$ (from eq. (A11)), and $\frac{h}{h'}$ from the equation

$$\frac{h}{h'} = \frac{1}{\frac{T_r - T_p}{T_r - T_p'} \lambda} \quad (A18)$$

(obtained from eqs. (A4), (A8), and (A11)) are also shown in the table.

The values of $\frac{h}{h'}$ in column ⑦ are actually the first approximation in an iterative procedure since h' and T_p' were used to obtain the values of λ . The final results, of course, depend directly on the accuracy of the surface temperatures of the plug and model wall. It is believed that the measured values of T_w (as shown for this example in fig. 2(d) and used in column ④) are too large because of the type of thermocouple installation, which was described in the section entitled "Hemisphere-cylinder heat-transfer model." The magnitude of this error can be estimated by assuming one-dimensional heat flow through the model wall of thickness Δr_m . The relation for the outside-wall temperature T_w (assuming $h = h'$) is then

$$T_w' = \frac{T_i + \frac{\Delta r_m}{k_{st}} h' T_r}{1 + \frac{\Delta r_m}{k_{st}} h'}$$

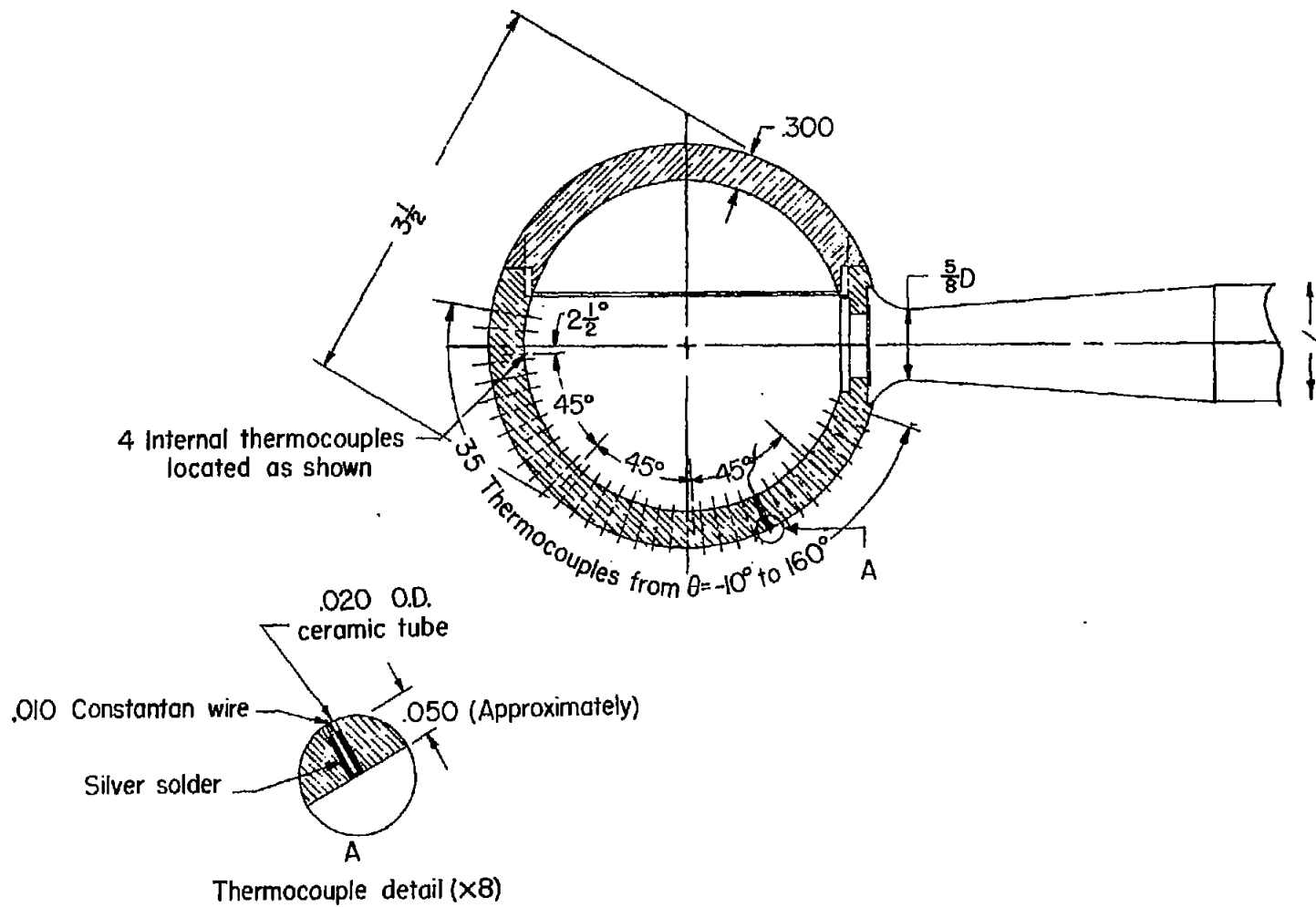
which was used to compute the values shown in column ⑧. These estimated values were then used to compute a new set of values for $\frac{h}{h'}$ given in column ⑨. For this particular test, then, the correction factor $\frac{h}{h'}$ varied from about 0.53 to 0.78.

In view of these possible errors in T_w and T_p and the conservative effect of the boundary conditions (eqs. (A13)), the correction factors shown in column ⑨ are believed to be somewhat small. Consideration of all pertinent effects indicates that most of the heat-meter data in this report should be multiplied by a correction factor of 0.8 with a probable uncertainty of ± 10 percent. However, when h is small, as at $\theta = 90^\circ$ on the hemisphere, the values of X_p are small and larger correction factors may be required. It was impractical to attempt to apply a correction to all the data because of possible unknown errors in T_w , T_p , and ϵ .

REFERENCES

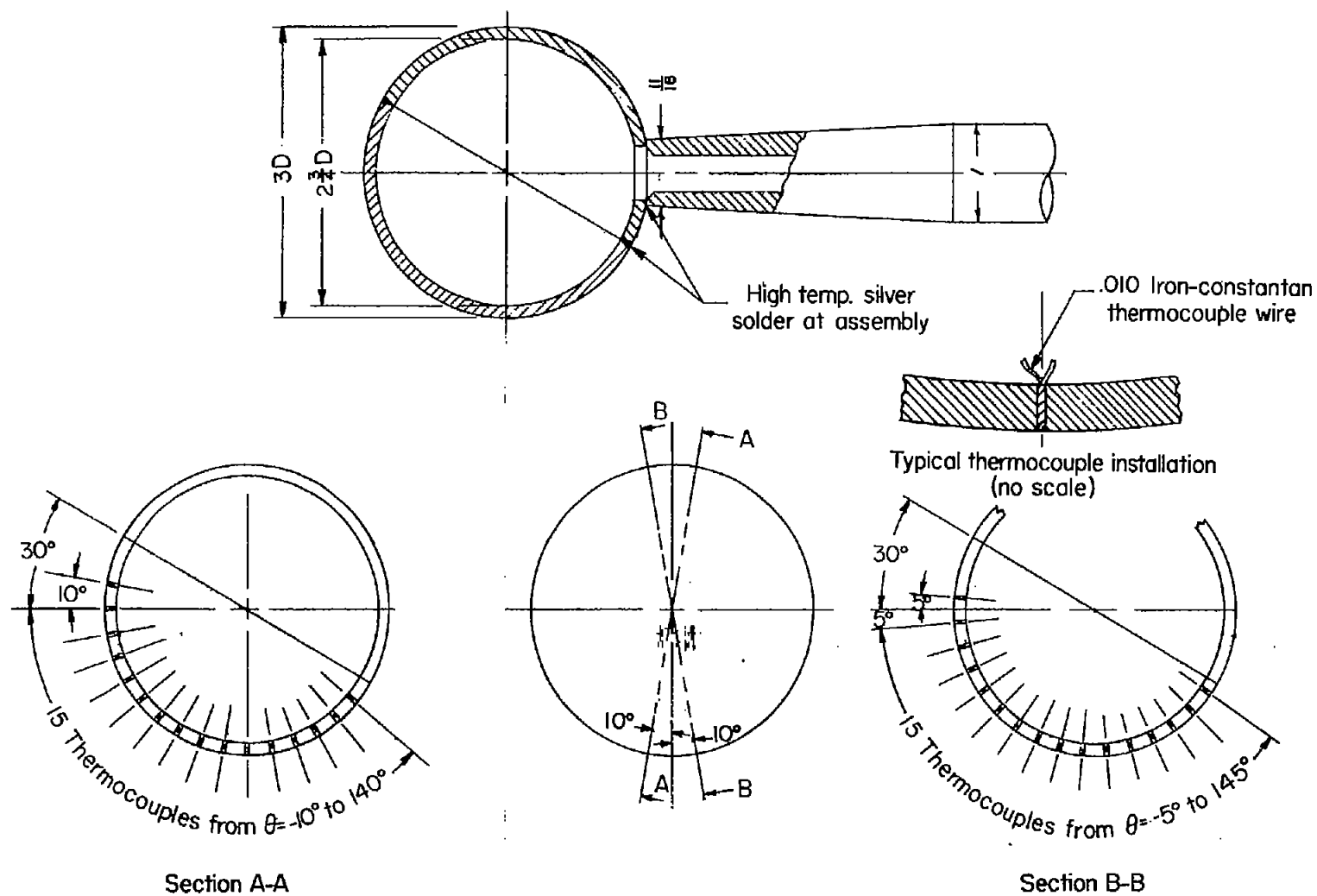
1. Korobkin, Irving: Local Flow Conditions, Recovery Factors and Heat-Transfer Coefficients on the Nose of a Hemisphere-Cylinder at a Mach Number of 2.8. NAVORD Rep. 2865 (Aeroballistic Res. Rep. 175), U. S. Naval Ord. Lab. (White Oak, Md.), May 5, 1953.
2. Chauvin, Leo T., and Maloney, Joseph P.: Experimental Convective Heat Transfer to a 4-Inch and 6-Inch Hemisphere at Mach Numbers From 1.62 to 3.04. NACA RM L53L08a, 1954.
3. Stalder, Jackson R., and Nielsen, Helmer V.: Heat Transfer From a Hemisphere-Cylinder Equipped With Flow-Separation Spikes. NACA TN 3287, 1954.
4. Stine, Howard A., and Wanlass, Kent: Theoretical and Experimental Investigation of Aerodynamic-Heating and Isothermal Heat-Transfer Parameters on a Hemispherical Nose With Laminar Boundary Layer at Supersonic Mach Numbers. NACA TN 3344, 1954.
5. Korobkin, Irving: Laminar Heat Transfer Characteristics of a Hemisphere for the Mach Number Range 1.9 to 4.9. NAVORD Rep. 3841 (Aeroballistic Res. Rep. 257), U. S. Naval Ord. Lab. (White Oak, Md.), Oct. 10, 1954.
6. Gruenewald, K. H., and Fleming, W. J.: Laminar Heat Transfer to a Hemisphere at Mach Number 3.2 and at Low Heat-Transfer Rates. NAVORD Rep. 3980 (Aeroballistic Res. Rep. 282), U. S. Naval Ord. Lab. (White Oak, Md.), Feb. 20, 1956.
7. Winkler, Eva M., and Danberg, J. E.: Heat Transfer Characteristics of a Hemisphere Cylinder at Hypersonic Mach Numbers. Preprint No. 622, S.M.F. Fund Preprint, Inst. Aero. Sci., Jan. 1956.
8. Crawford, Davis H., and McCauley, William D.: Investigation of the Laminar Aerodynamic Heat-Transfer Characteristics of a Hemisphere-Cylinder in the Langley 11-Inch Hypersonic Tunnel at a Mach Number of 6.8. NACA TN 3706, 1956.
9. Reshotko, Eli, and Cohen, Clarence B.: Heat Transfer at the Forward Stagnation Point of Blunt Bodies. NACA TN 3513, 1955.
10. Hilsenrath, Joseph, Beckett, Charles W., et al.: Tables of Thermal Properties of Gases. NBS Cir. 564, U. S. Dept. Commerce, 1955.

11. Beckwith, Ivan E.: Heat Transfer and Skin Friction by an Integral Method in the Compressible Laminar Boundary Layer With a Streamwise Pressure Gradient. NACA TN 3005, 1953.
12. Mangler, W.: Compressible Boundary Layers on Bodies of Revolution. Reps. and Translations No. 47, British M.A.P. Völkenrode, Mar. 15, 1946.
13. Falkner, V. M.: A New Law for Calculating Drag - The Resistance of a Smooth Flat Plate With Turbulent Boundary Layer. Aircraft Engineering, vol. XV, no. 169, Mar. 1943, pp. 65-69.
14. Sommer, Simon C., and Short, Barbara J.: Free-Flight Measurements of Turbulent-Boundary-Layer Skin Friction in the Presence of Severe Aerodynamic Heating at Mach Numbers From 2.8 to 7.0. NACA TN 3391, 1955.
15. Seiff, Alvin: Examination of the Existing Data on the Heat Transfer of Turbulent Boundary Layers at Supersonic Speeds From the Point of View of Reynolds Analogy. NACA TN 3284, 1954.
16. Cohen, Clarence B., and Reshotko, Eli: The Compressible Laminar Boundary Layer With Heat Transfer and Arbitrary Pressure Gradient. NACA Rep. 1294, 1956. (Supersedes NACA TN 3326.)
17. Dryden, Hugh L.: Review of Published Data on the Effect of Roughness on Transition From Laminar to Turbulent Flow. Jour. Aero. Sci., vol. 20, no. 7, July 1953, pp. 477-482.



(a) Isothermal heat-transfer model.

Figure 1.- Sketches of models and instrumentation used in the investigation. All dimensions are in inches unless otherwise indicated.



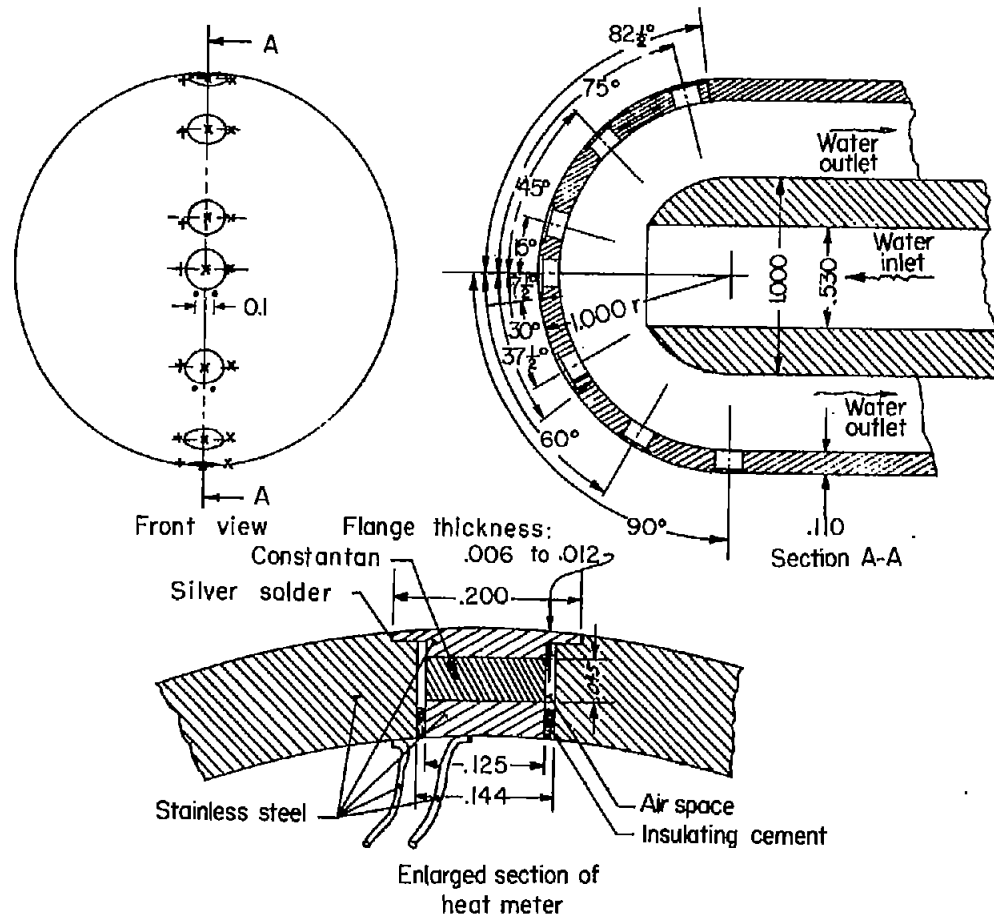
(b) Equilibrium-temperature model.

Figure 1.- Continued.

Copper - constantan
thermocouple junctions

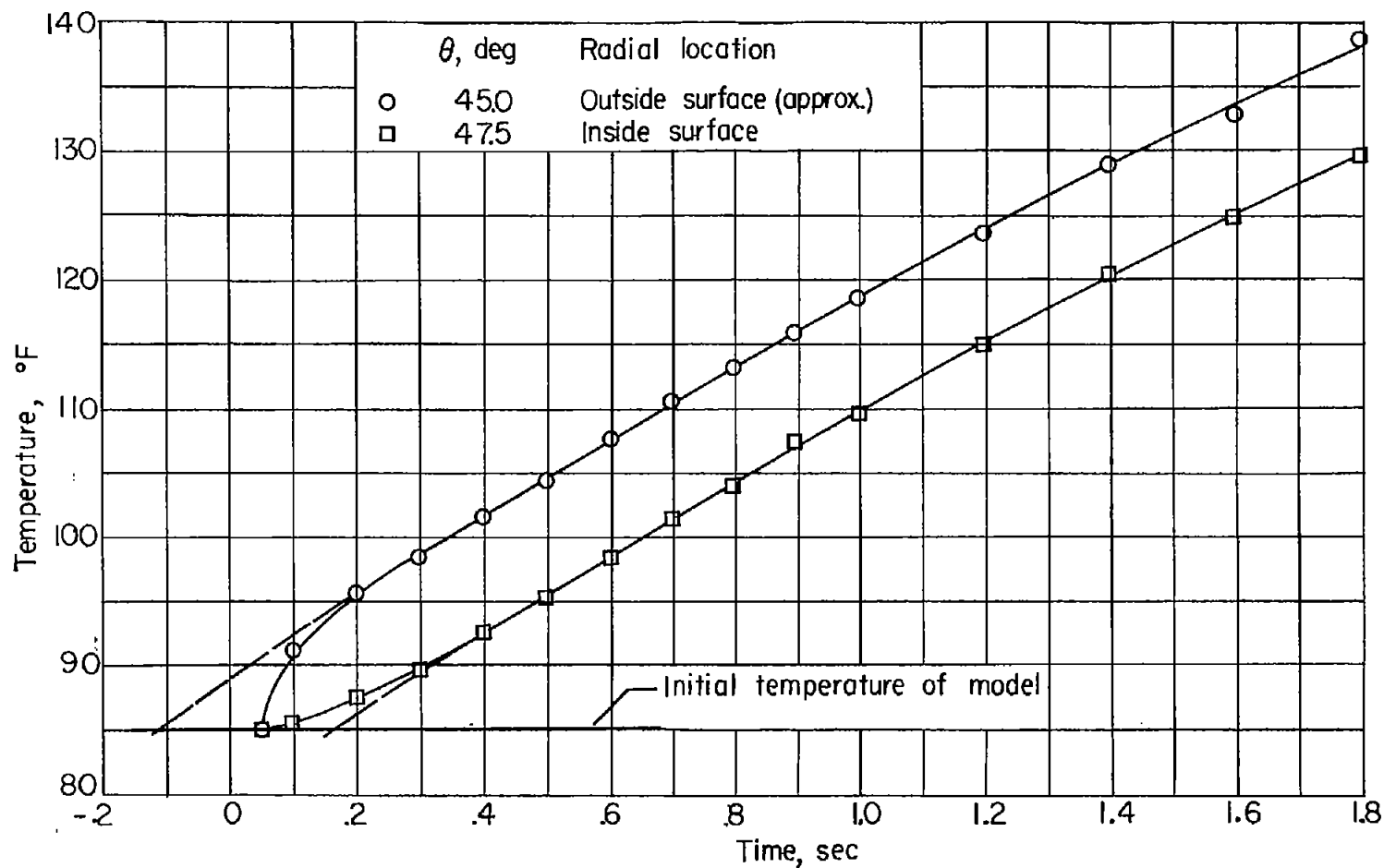
- + Inside surface
- Outside surface

Heat-meter leads
x Stainless steel



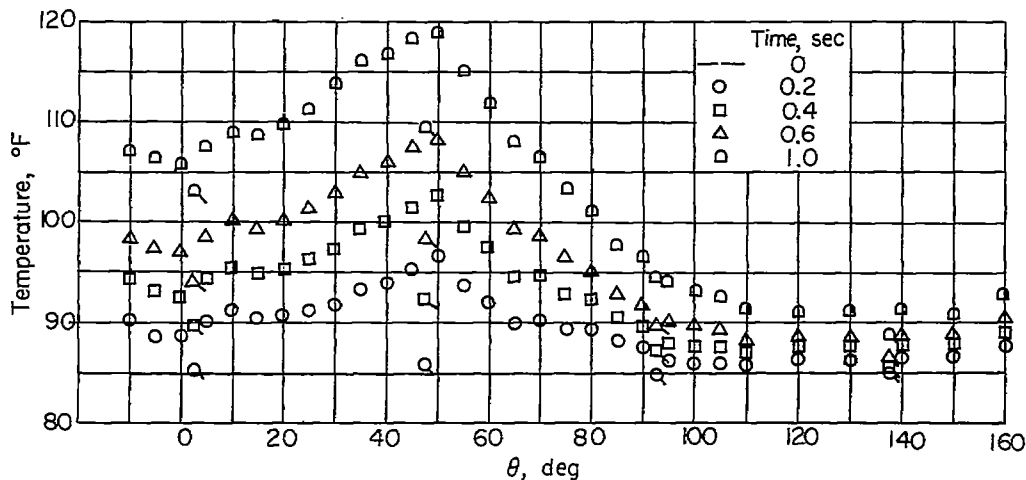
(c) Hemisphere-cylinder heat-transfer model and heat meter.

Figure 1.- Concluded.

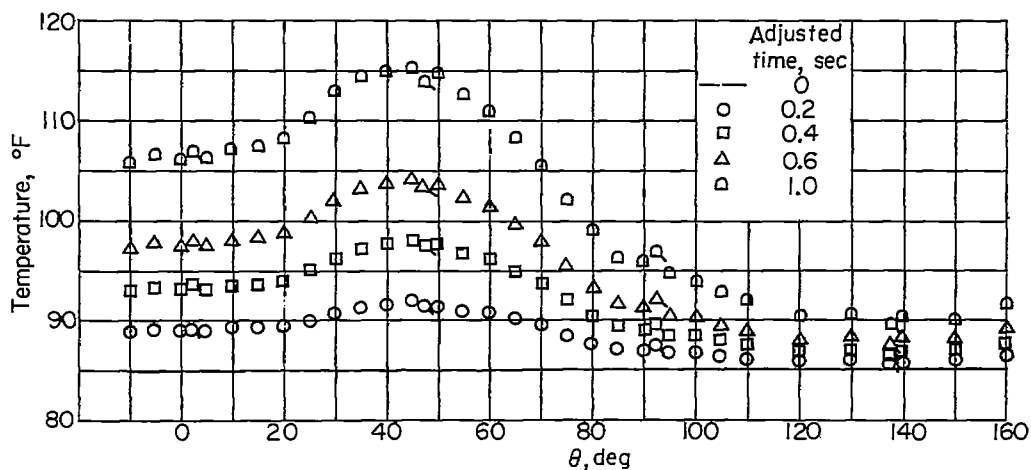


(a) Recorded temperature variation with time on the inside and outside surfaces at about the same θ station. $M_\infty = 2.0$; $p_0 = 98$ lb/sq in. abs; $T_0 = 492^\circ$ F; $R_\infty = 3.4 \times 10^6$ (rough surface).

Figure 2.- Temperature distributions on the heat-transfer models for typical tests.

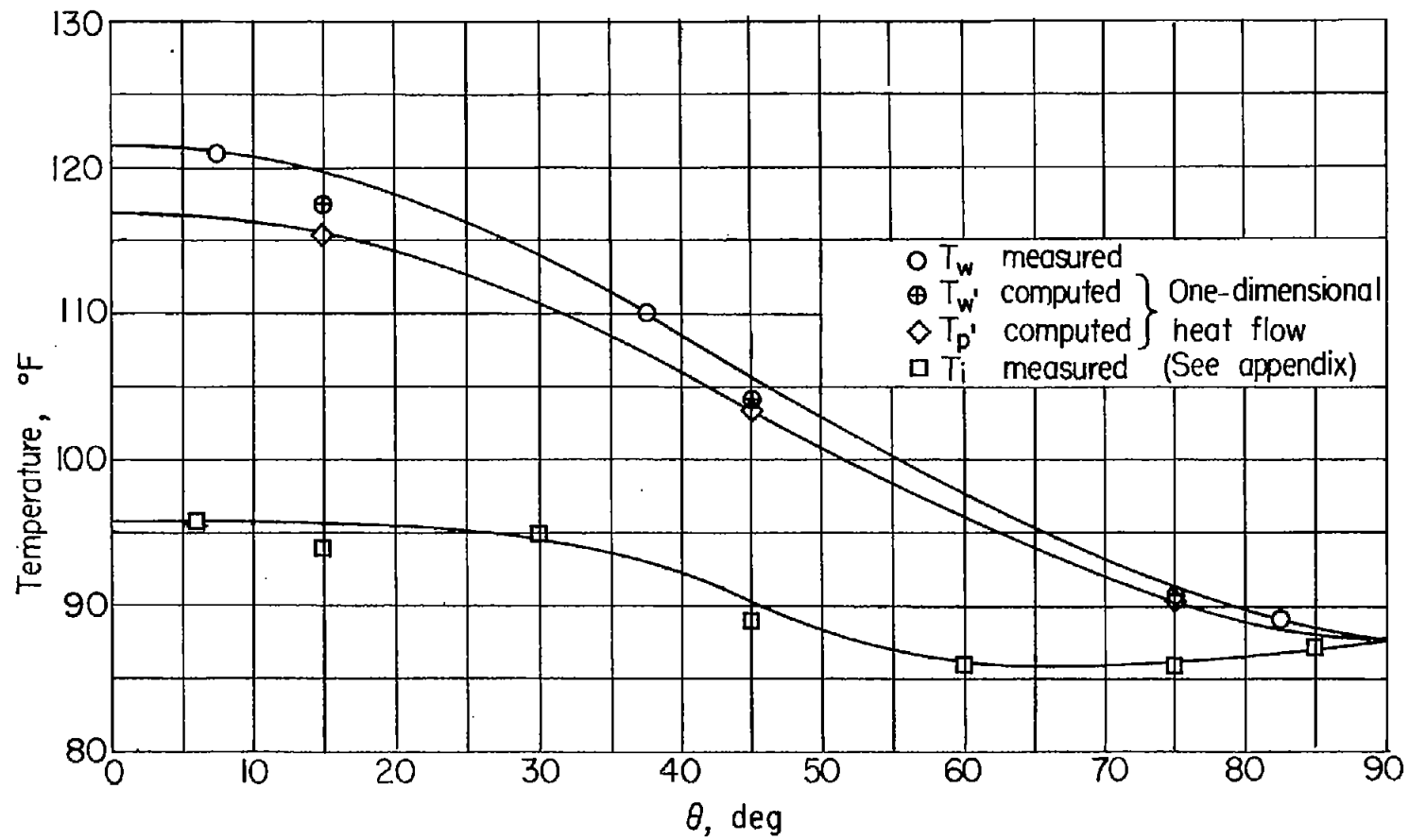


- (b) Temperature-time history of the copper sphere as read directly from the records. Flagged symbols denote temperatures measured at the inside surface; all other values are measured about 0.05 inch from the outside surface. $M_\infty = 2.0$; $p_0 = 98$ lb/sq in. abs; $T_0 = 492^\circ$ F; $R_\infty = 3.4 \times 10^6$ (rough surface).



- (c) Temperature time history of the copper sphere for the same test shown in figure 2(a) but corrected for the effect of thermocouple depth.

Figure 2.- Continued.



(d) Temperature distribution on the inside and outside surfaces of the hemisphere-cylinder heat-meter model. $M_\infty = 4.15$; $p_0 = 324$ lb/sq in. abs; $T_0 = 241^\circ$ F; $R_\infty = 3.2 \times 10^6$ (polished surface).

Figure 2.- Concluded.

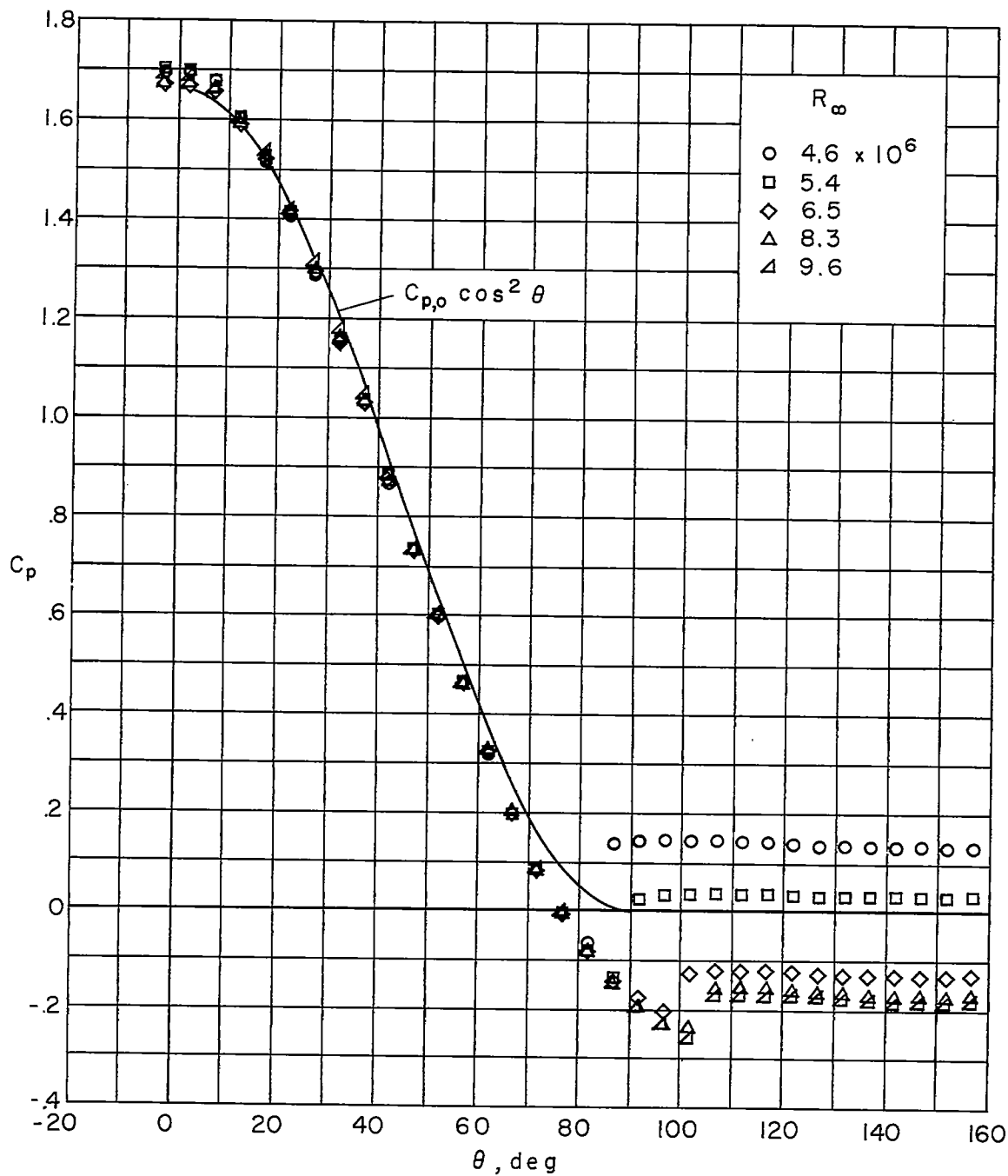


Figure 3.- Distribution of the pressure coefficient around the sphere at $M_o = 2.00$ for various stream Reynolds numbers.

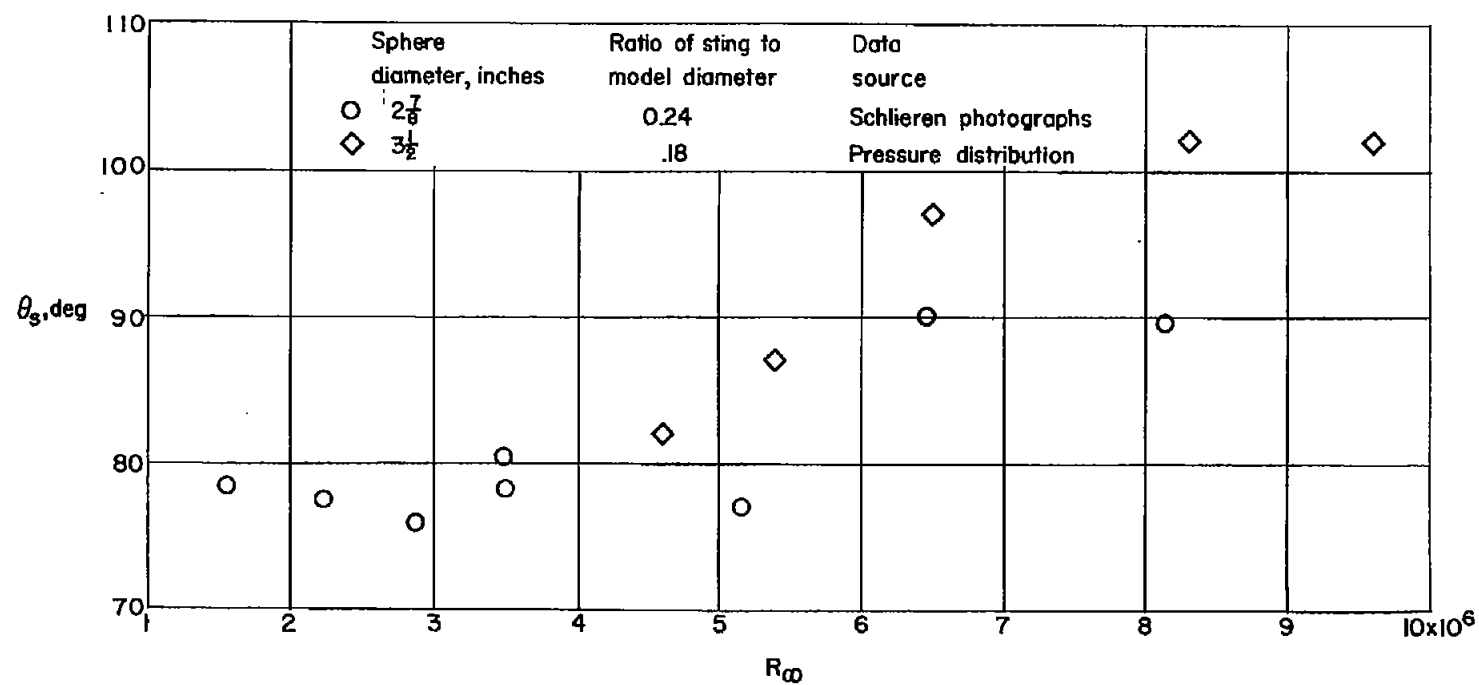


Figure 4.- Variation of the separation point with stream Reynolds number on two of the models at $M_\infty = 2.0$.



No flow

 $R_{\infty} = 1.56 \times 10^6$  $R_{\infty} = 5.16 \times 10^6$  $R_{\infty} = 8.13 \times 10^6$

L-57-2730

Figure 5.- Schlieren photographs of the recovery-temperature model at $M_{\infty} = 2.0$ and three stream Reynolds numbers.

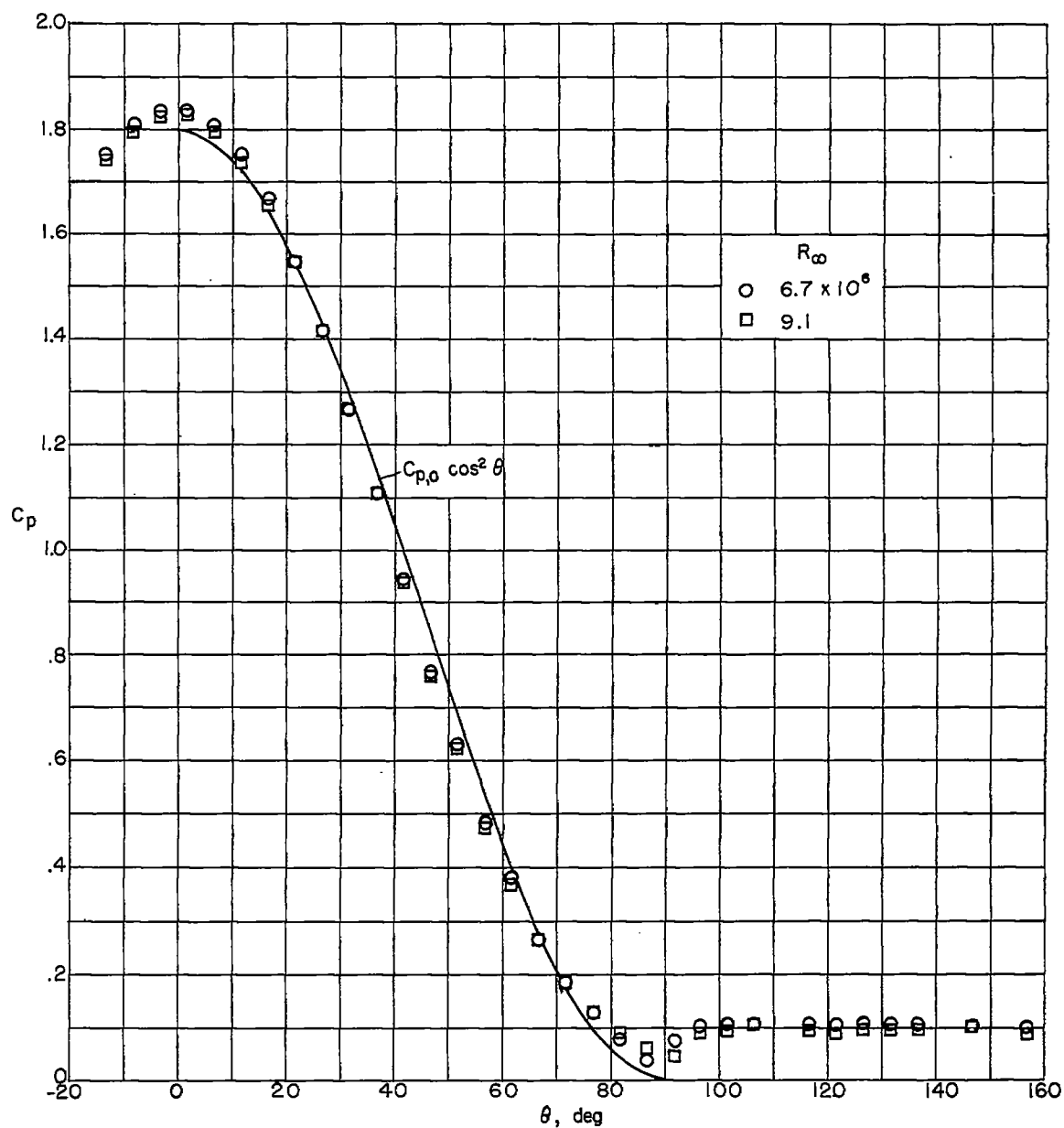


Figure 6.- Distribution of the pressure coefficient around the sphere at $M_\infty = 4.15$ for two stream Reynolds numbers.

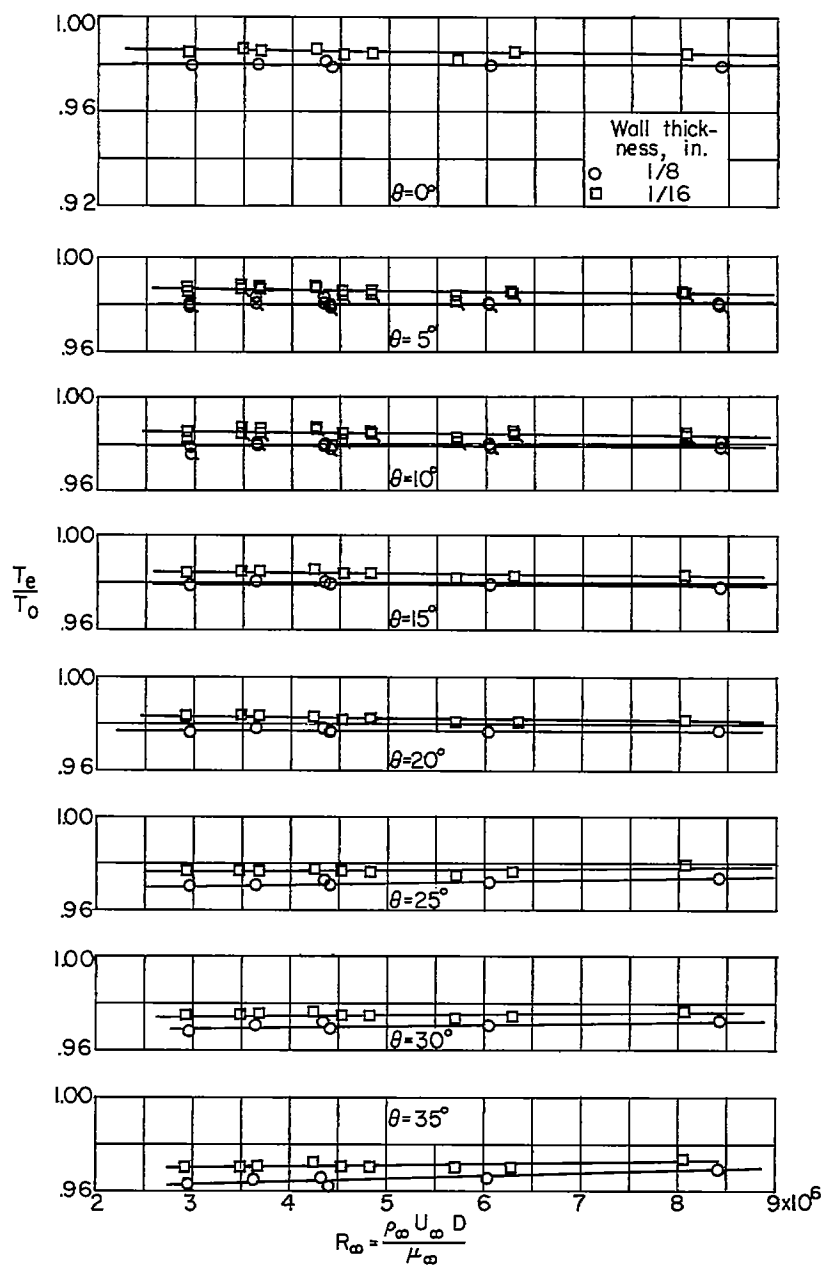
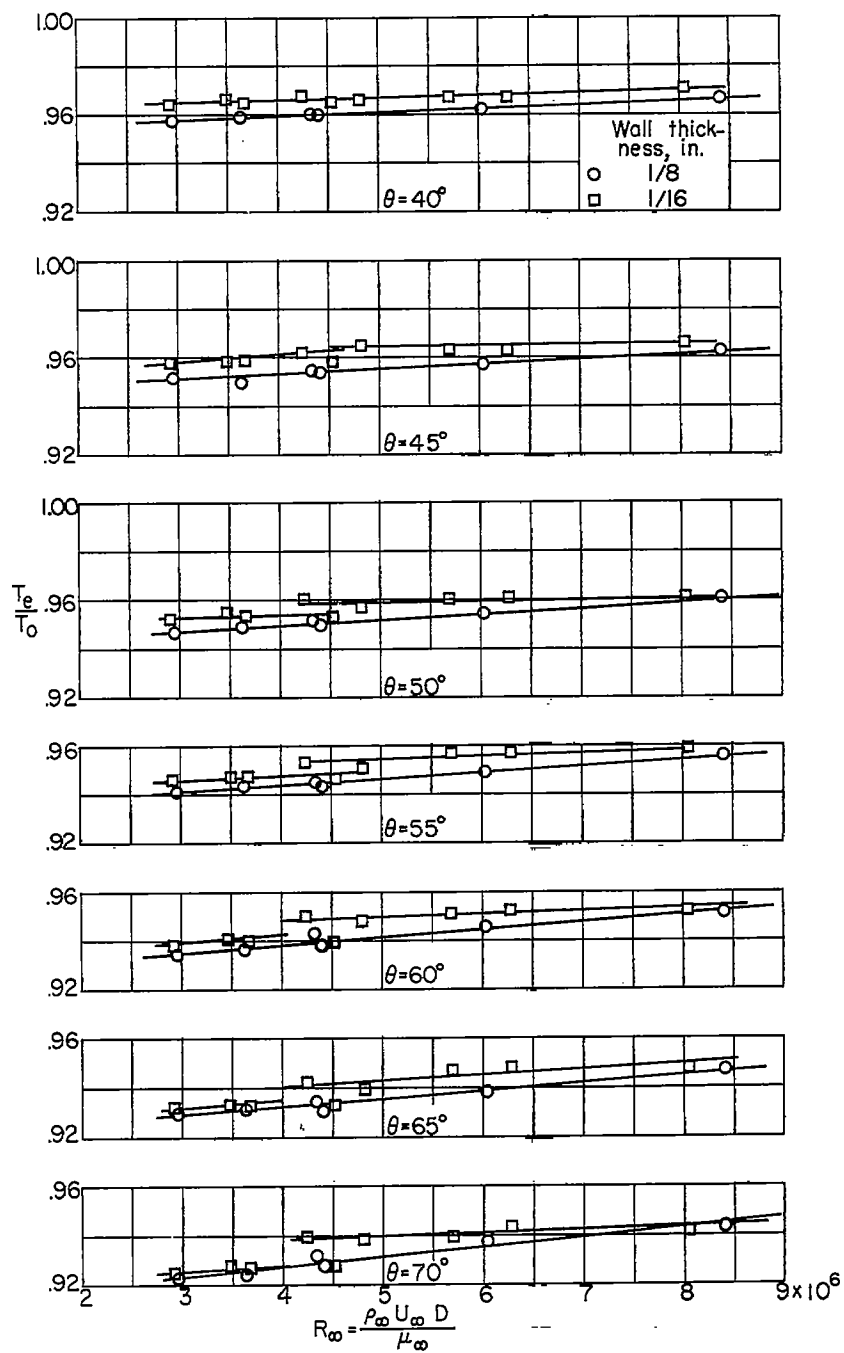
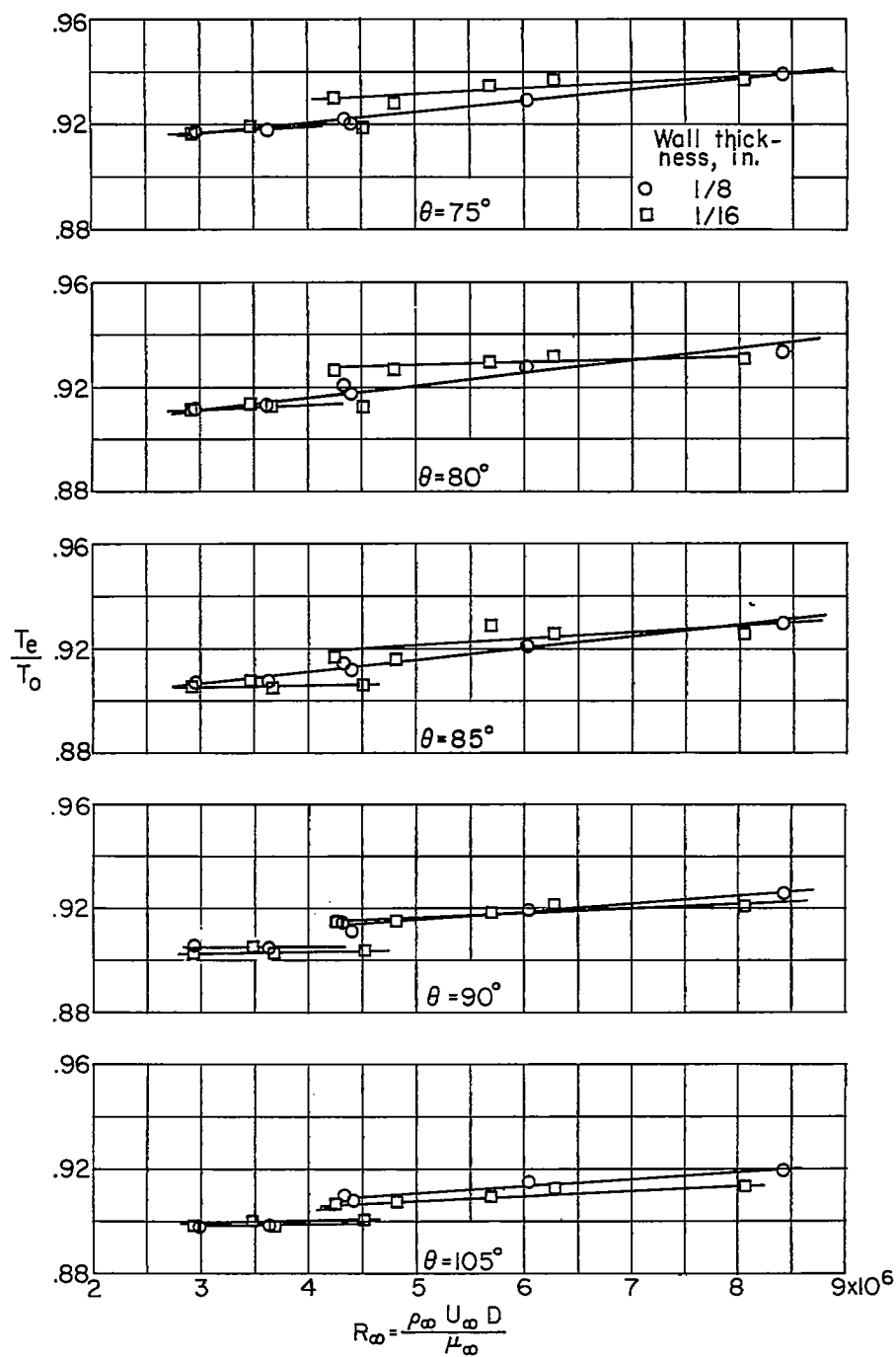
(a) $\theta = 0^\circ$ to 35° .

Figure 7.- Variation with stream Reynolds number of the ratio of the equilibrium temperature to the stagnation temperature at $M_\infty = 4.15$ for two wall thicknesses. Flagged symbols denote negative values of θ .



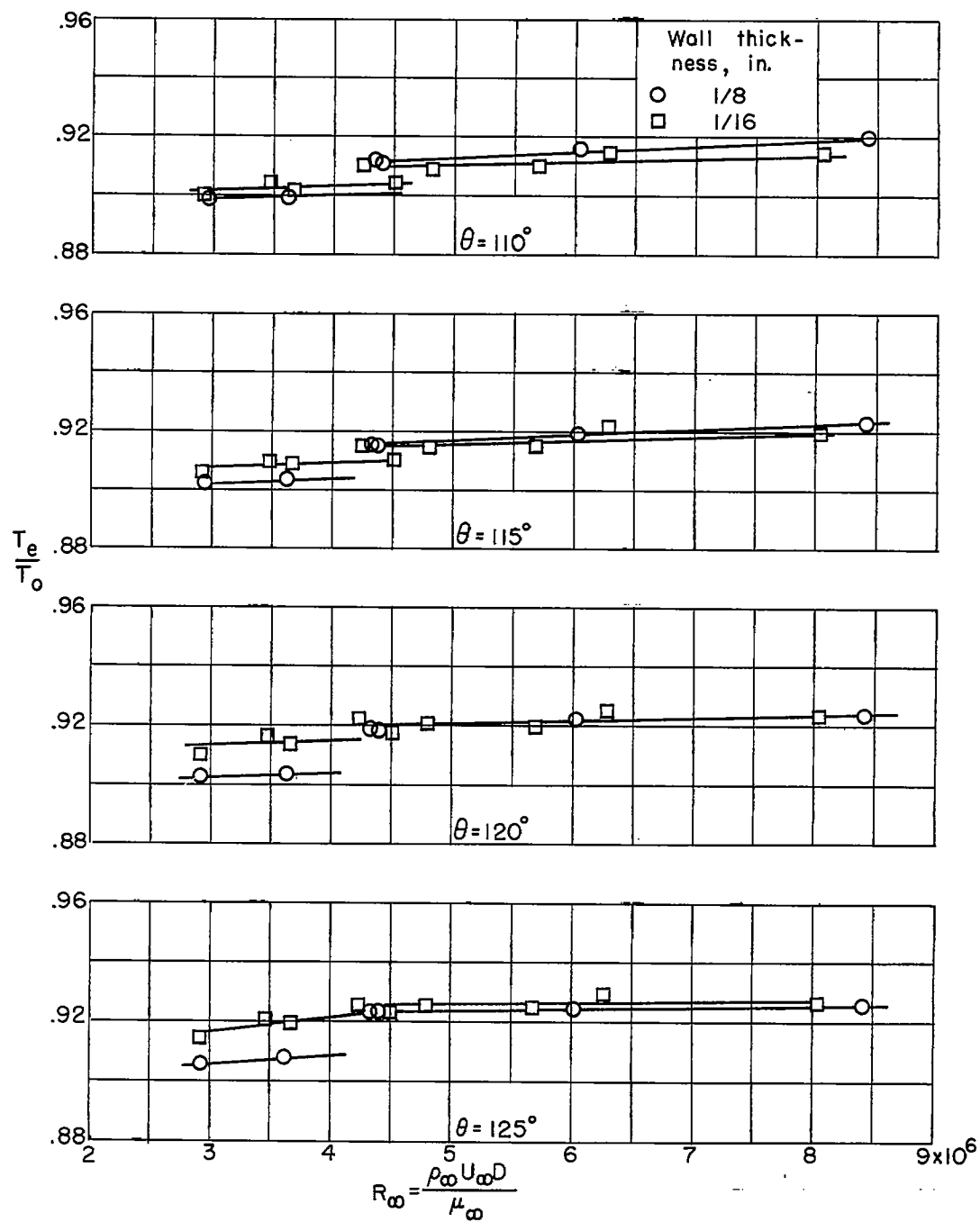
(b) $\theta = 40^\circ$ to 70° .

Figure 7.- Continued.



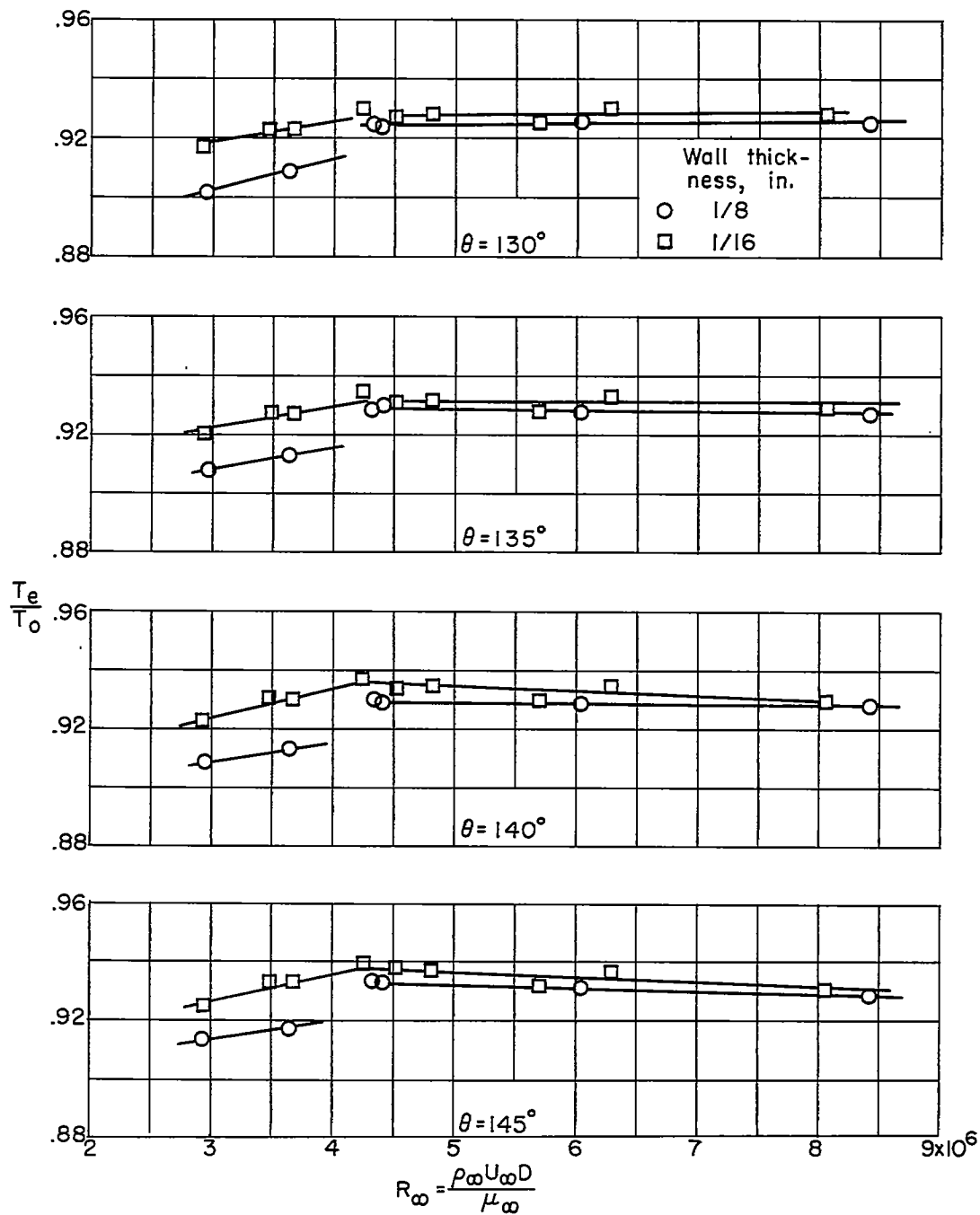
(c) $\theta = 75^\circ$ to 105° .

Figure 7.- Continued.



(d) $\theta = 110^\circ$ to 125° .

Figure 7.- Continued.



(e) $\theta = 130^\circ$ to 145° .

Figure 7.- Concluded.

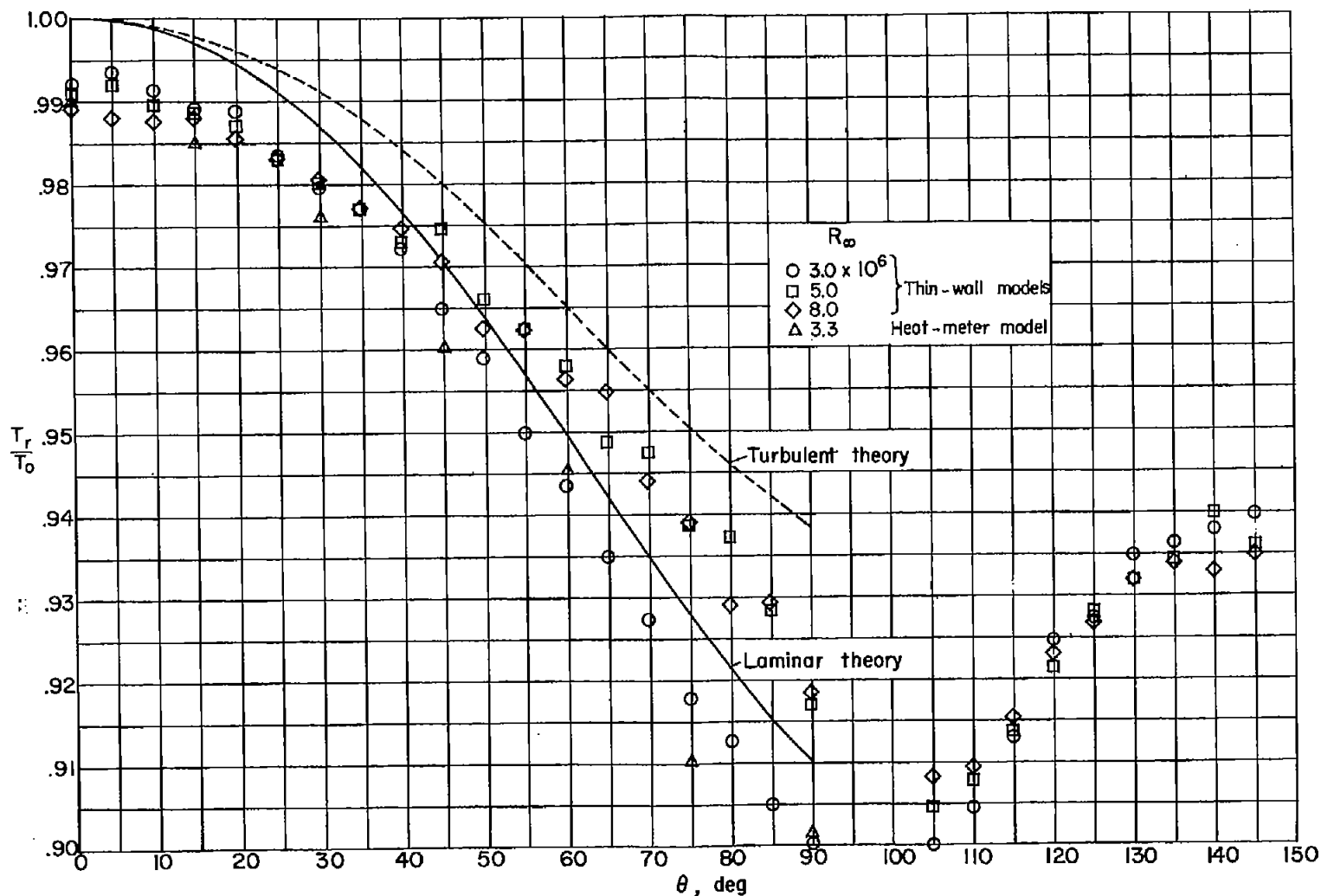


Figure 8.- Variation with θ of the ratio of the recovery temperature to the stagnation temperature at $M_\infty = 4.15$ for three Reynolds numbers.

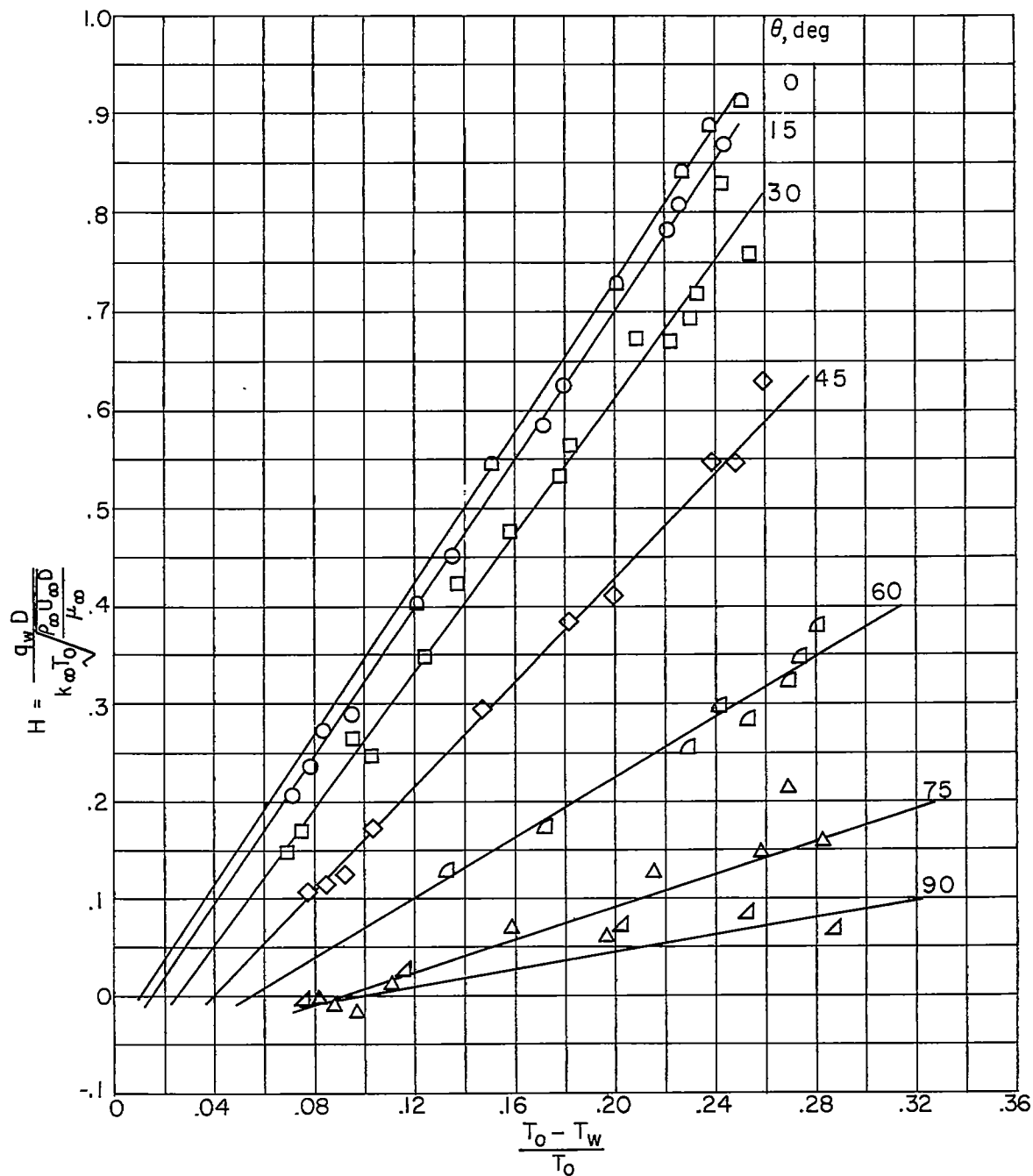


Figure 9.- Variation of heat-transfer parameter with wall-temperature parameter for various values of θ on the heat-meter model at $M_\infty = 4.15$ and $R_\infty \approx 3.3 \times 10^6$.

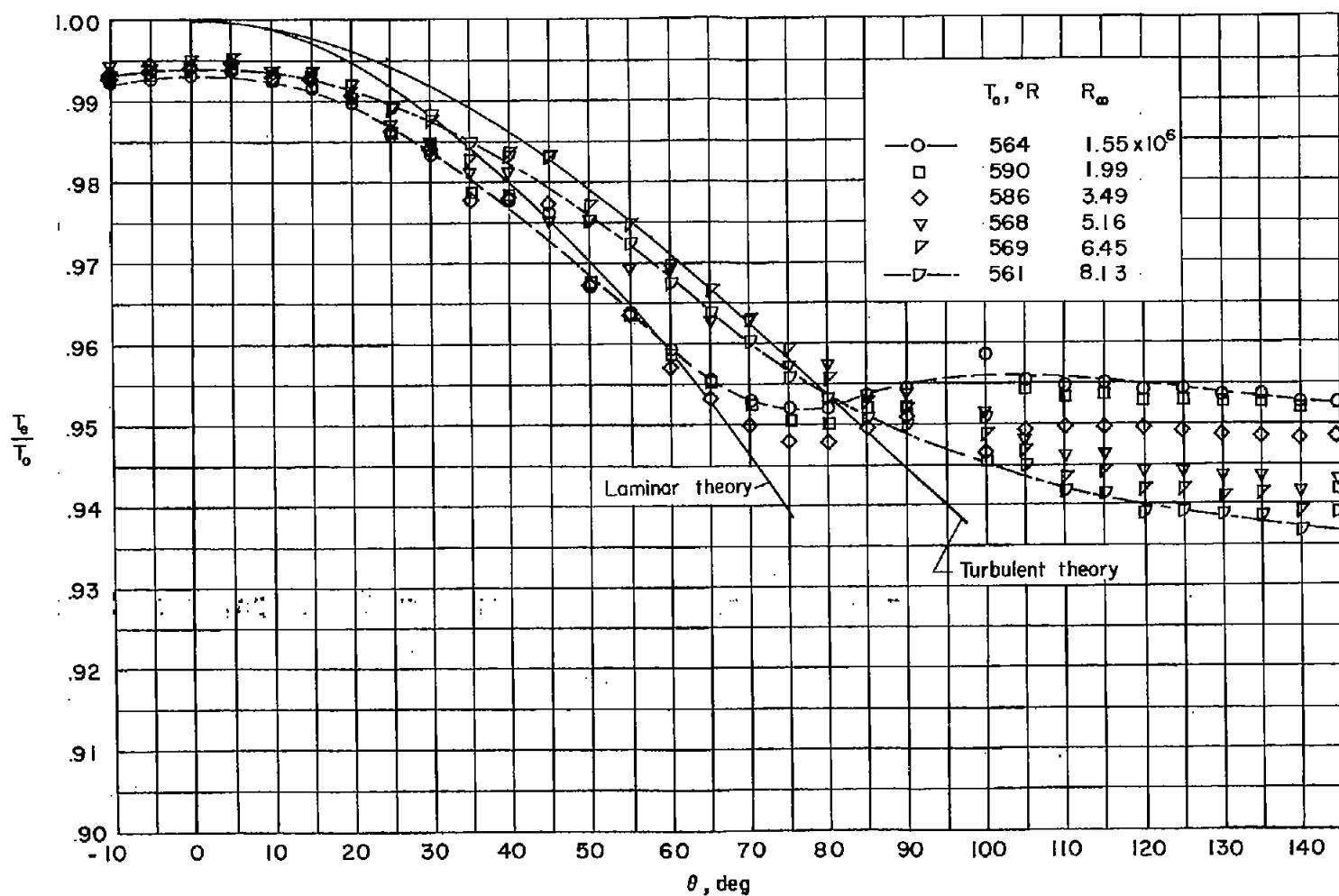


Figure 10.- Ratio of the equilibrium temperature to the stagnation temperature at $M_0 = 2.00$ and several Reynolds numbers.

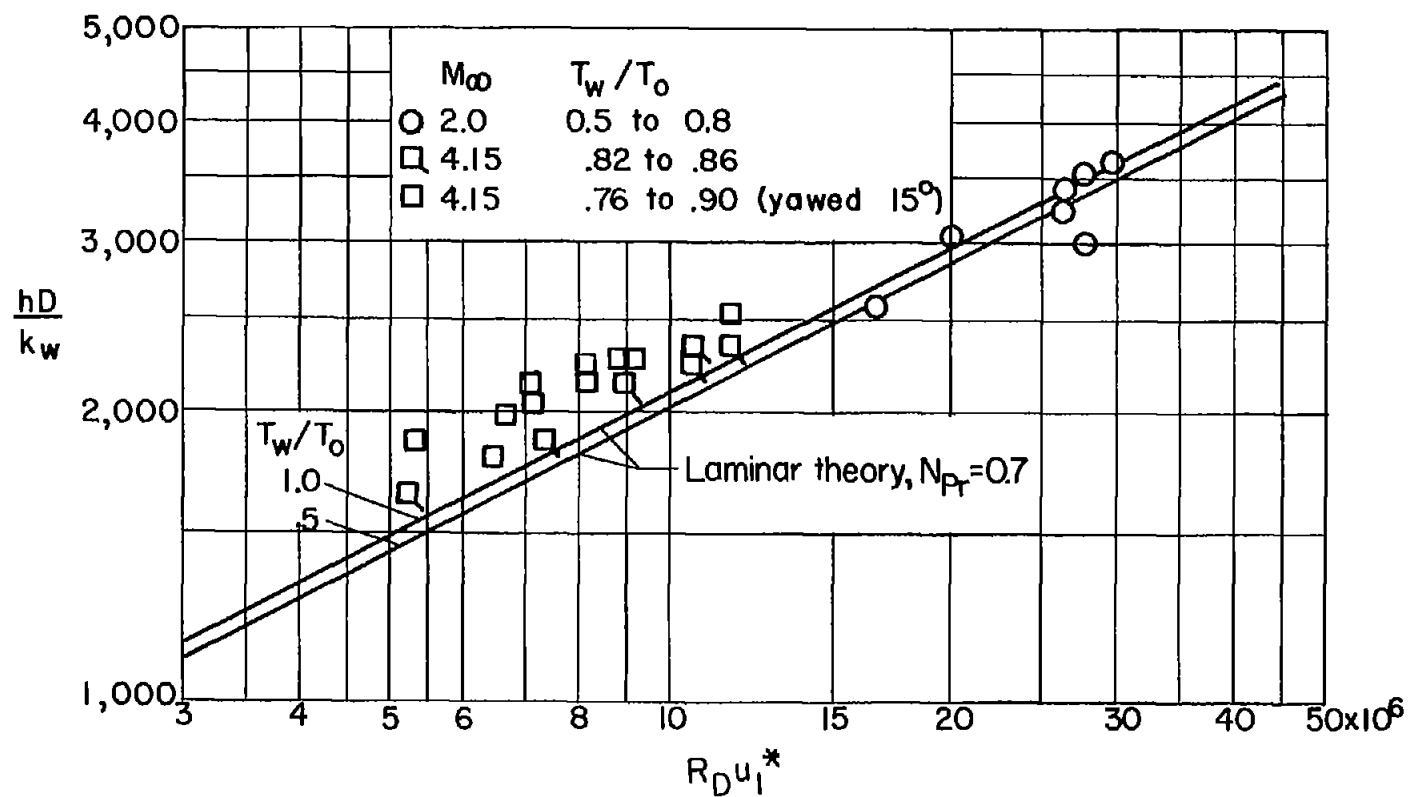


Figure 11.- Variation of Nusselt number at the stagnation point with the product of Reynolds number and the dimensionless velocity gradient.

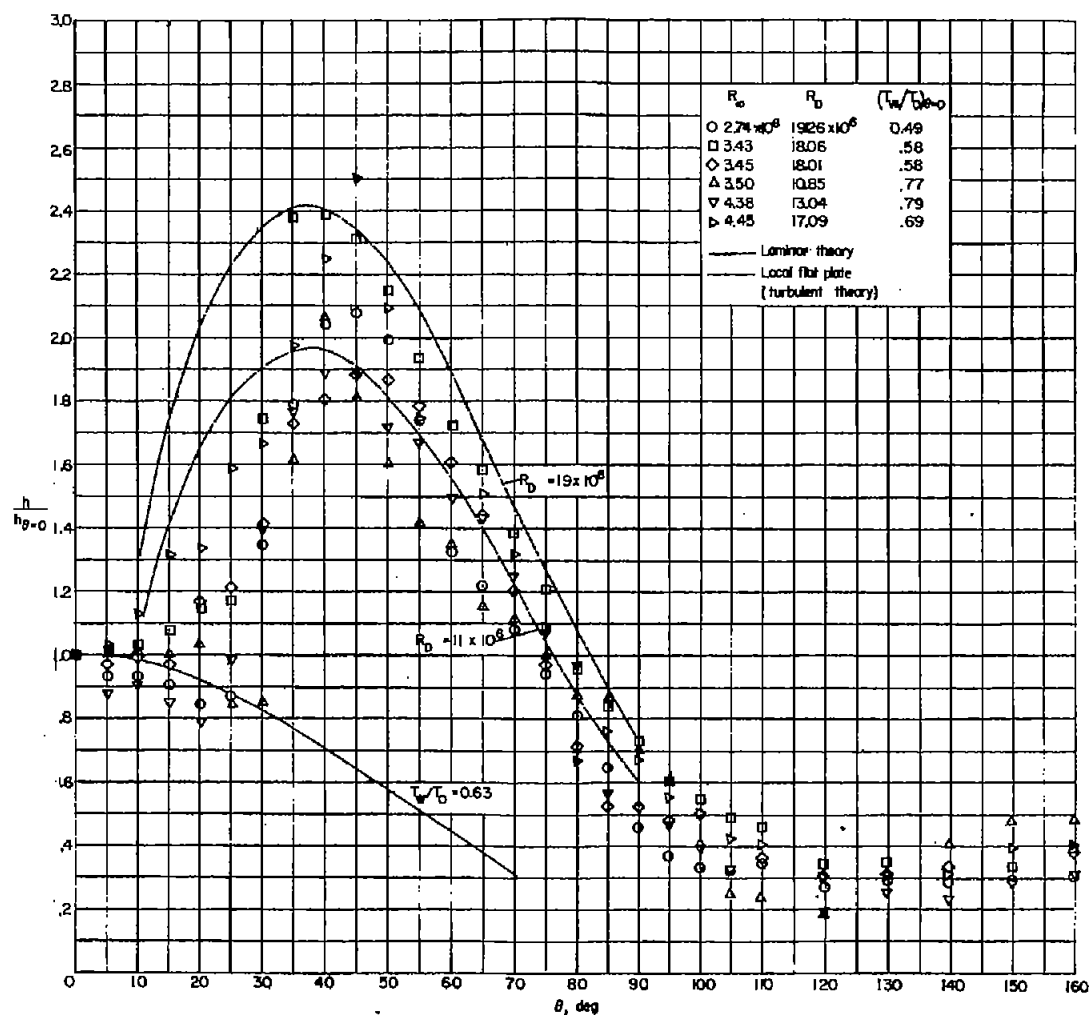


Figure 12.- Variation with θ of the ratio of the local heat-transfer coefficient to the value at the stagnation point at $M_{\infty} = 2.0$ and several stream Reynolds numbers.

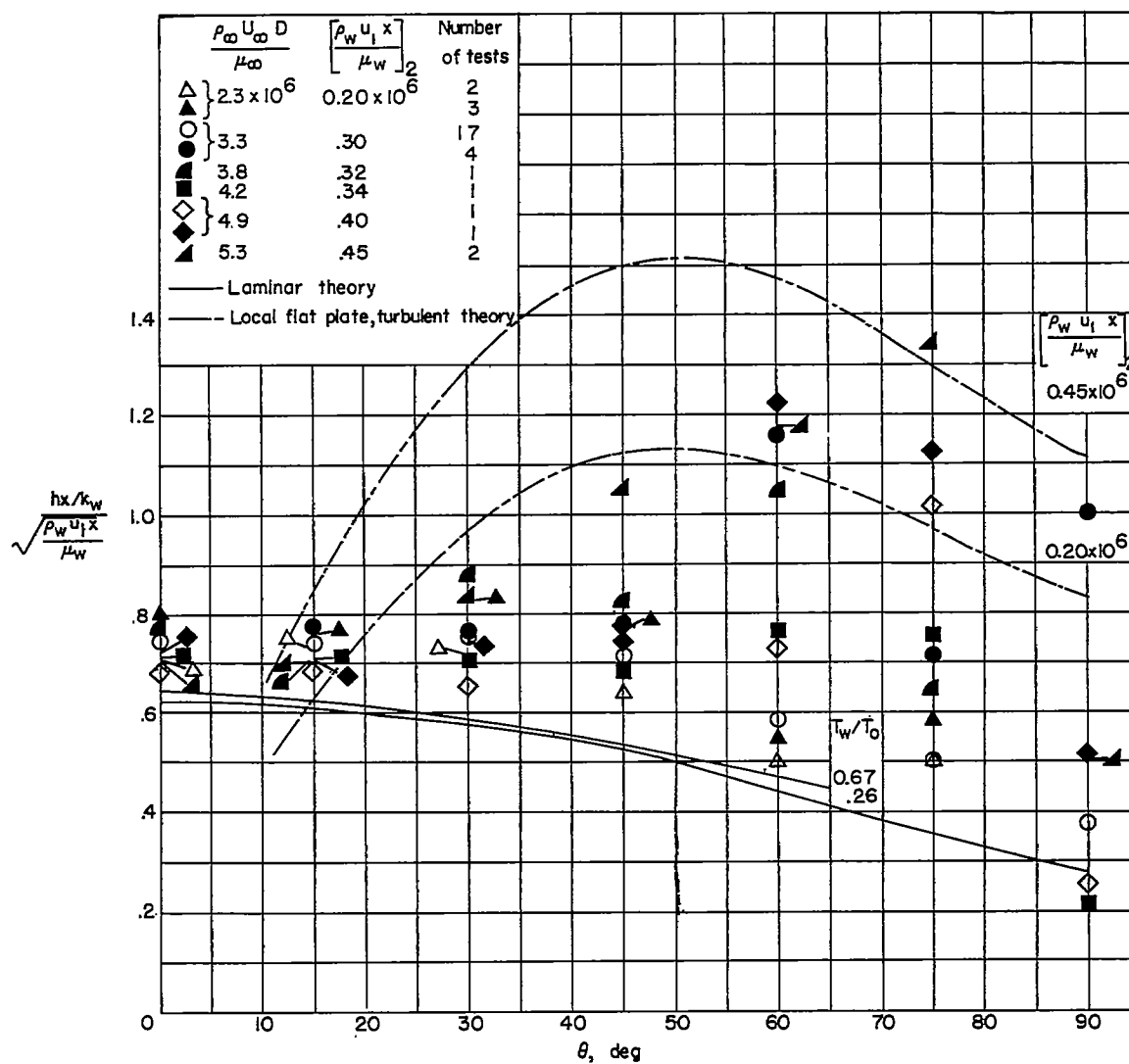


Figure 13.- Local Nusselt number divided by the square root of local Reynolds number at $M_\infty = 4.15$. The solid symbols denote tests made without polishing between tests.

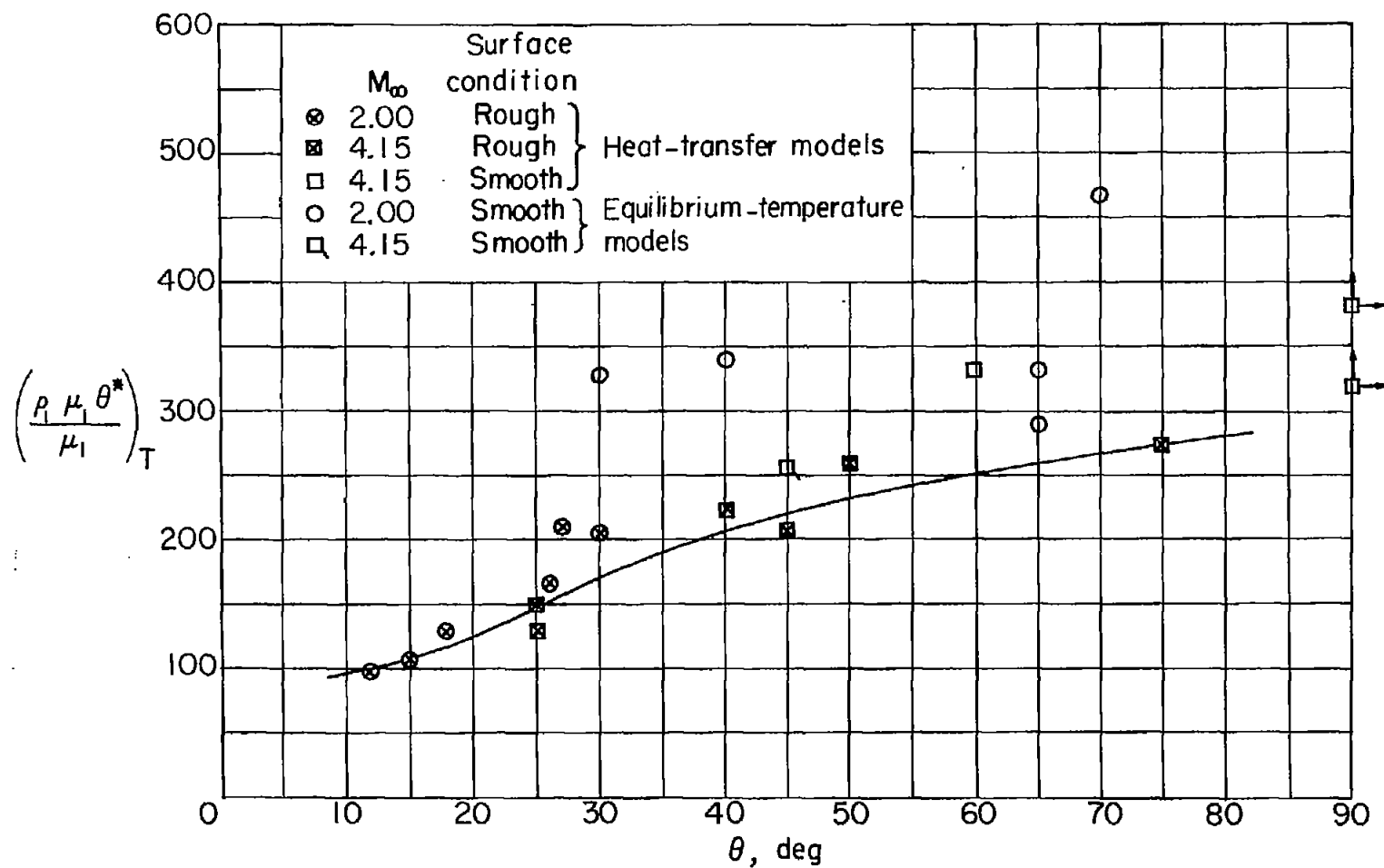


Figure 14.- Variation of momentum-thickness Reynolds number at transition with θ .

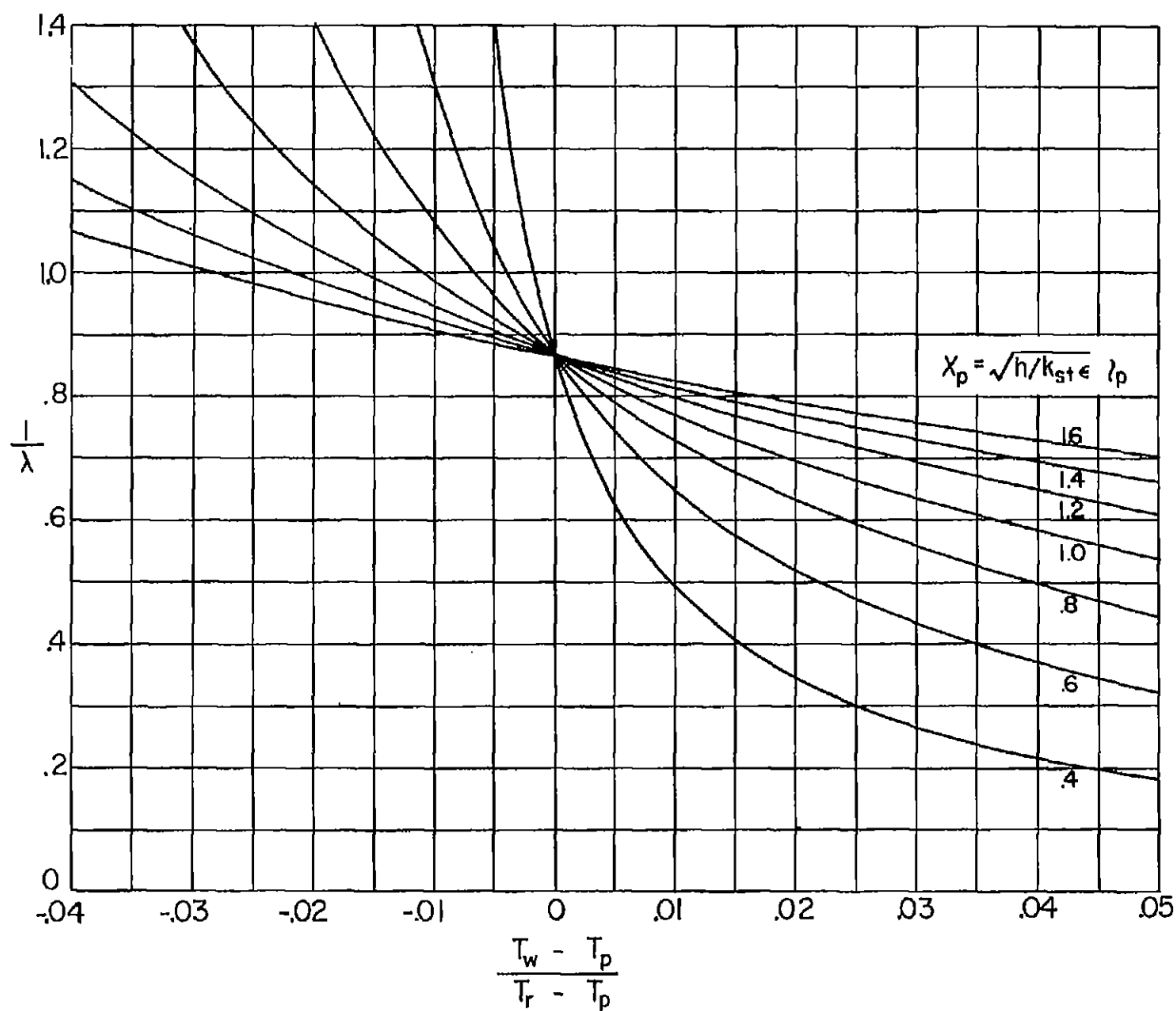


Figure 15.- Calculated variation of a correction factor which is used to obtain the ratio of corrected to indicated heat-transfer coefficients for the heat meter.